Computational analysis of unsteady flow features around a realistic Estate vehicle with hybrid RANS/LES methods

Francois Delassaux, Iraj Mortazavi, Vincent Herbert, Charles Ribes

Computational analysis of unsteady flow features around a realistic Estate vehicle with hybrid RANS/LES methods

Francois Delassaux, Iraj Mortazavi, Vincent Herbert & Charles Ribes

Abstract A comparative study is conducted to analyze the flow around a realistic Peugeot Estate car (308 SW) using RKE and SST RANS models, as well as DDES hybrid RANS/LES approach. The authors used previous work on 25° Ahmed bodies to establish the best grid and DDES parameters for external aerodynamics prediction. The aim of this work is to extend and transpose the numerical methodology to a realistic car. Numerical and physical characteristics related to the simulation of this complex flow are therefore carefully investigated. The numerical results are compared to in-house experiments carried out in S2A Stellantis Wind Tunnel. Two grids with 115 and 185 million elements, based on 20 prism layers cells near the wall, are used to compare the three turbulence models. Even with a smaller grid size in the wake and underbody, the predictions of drag and lift coefficients are almost identical. Moreover, refining the near-wall region from 20 to 30 prism layers has no effect on drag coefficient and flow prediction. Consequently, the grid with 20 prism layers and 115M cells is used as reference grid in this work. Then, the flow features between RKE, SST and SST DDES models are compared to two-dimensional (2D) and three-dimensional (3D) experimental results. RANS gives better agreement on aerodynamics forces. However, DDES reproduces accurately the specific three-dimensional topology of the flow around the car, in the wake and the underbody when RANS results are globally wrong.

Key words: turbulence modeling, hybrid RANS/LES methods, SST DDES, numerical method, real Estate vehicle, wake flow structures, drag coefficient.

Nomenclature

Δx^+	Dimensionless cell distance in streamwise direction
Δy^+	Dimensionless cell distance in spanwise direction
Δz^+	Dimensionless wall distance in vertical direction
δ	Boundary layer thickness
Δ_{max}	Maximum local grid spacing in the 3 directions
ν	Kinematic viscosity
ν_t	Turbulent viscosity
BCD	Bounded Central Differencing scheme
C_d	Drag coefficient
C_l	Lift coefficient
C_p	Pressure coefficient
$CAFE$	Corporate Average Fuel Economy
CD	Central Differencing scheme
CFD	Computational Fluid Dynamics
CFL	Courant Friedrichs Levy number
CPU	Central Processing Unit

Francois Delassaux - Iraj Mortazavi
Equipe M2N, CNAM Paris, 2 rue Conté, 75003 Paris, FRANCE
e-mail: francois.delassaux@gmail.com and iraj.mortazavi@lecnam.net

Vincent Herbert - Charles Ribes
Stellantis, Route de Gisy, 78943 Velizy-Villacoublay, FRANCE

$DDES$ Delayed Detached Eddy Simulation
DNS Direct Numerical Simulation
EV Electric Vehicle
EWT Enhanced Wall Treatment
GIS Grid Induced Separation
GPU Graphics Processing Unit
H_{AB} Ahmed body height
H_V Vehicle height
HPC High-Performance Computing
I Turbulent intensity
$IDDES$ improved Delayed Detached Eddy Simulation
L_{AB} Ahmed body length
L_V Vehicle length
LES Large Eddy Simulation
MSD Modeled Stress Depletion
$PANS$ Partial Averaged Navier-Stokes
PIV Particle Image Velocimetry
r Ratio between Δ_{max} over δ for DDES model
$RANS$ Reynolds-Averaged Navier-Stokes
Re_L Reynolds number based on the length of the vehicle
RKE Realizable k-ε
SAS Scale-Adaptive Simulation
$SBES$ Stress-Blended Eddy Simulation
SKE Standard k-ε
SRS Scale Resolving Simulation
SST Shear Stress Transport
V_∞ Free-stream velocity
W_{AB} Ahmed body width
W_V Vehicle width
$WFLES$ Wall-Function Large Eddy Simulation
$WLTP$ Worldwide harmonized Light vehicles Test Procedures
$WMLES$ Wall-Modeled Large Eddy Simulation
$WRLES$ Wall-Resolved Large Eddy Simulation

1 Introduction

The automotive industry is facing drastic restrictions on Greenhouse gas emissions. The European "CAFE" objective requires every car to meet a mean global CO_2 emission of 95 g/km on the 2021-2024 period. Emissions must be reduced by 15% on the 2025-2029 period. To achieve these goals, several components of the vehicle must be improved including greener engines, global mass reduction and improved aerodynamics performances. Indeed, aerodynamics plays a key role in acheiving these objectives. Bluff body flows are characterized by regions of separated flows containing a wide range of turbulent scales. These regions are mainly responsible for drag and lift forces applied on the body. Improving aerodynamics and therefore reducing drag can significantly reduce fuel consumption or increase the range of Electric Vehicle batteries. To improve aerodynamics, experiments and CFD are two required and complementary tools. Due to the expensive cost of wind tunnel sessions, turbulence modeling must replace experiments in the near future. Moreover, CFD allows for better flexibility and speed of reaction to change geometries and carry on many tests in a shorter duration of time. Furthermore, the new Worldwide Harmonized Light Vehicles Test Procedure (WLTP) norm is far more restrictive for automotive manufacturers compared to the previous one. Indeed, each car configuration, for example, a wheel rim change or the addition of a rear spoiler, must be quantified (in terms of drag and lift) by the manufacturer. This new norm reinforces the use of CFD and requires predictive numerical methodology.

Due to low computer power at the early stages of CFD and the lack of wind tunnel facilities, the scientist community was not able to fully study the aerodynamics of realistic vehicles. They had to developed simplified car geometries. We can cite a non-exhaustive list of them: the Ahmed body in 1984 [2], a two-dimensional car model in 1996 [3], a SAE model [9] and more recently, the Windsor model in 2019 [51]. All of these geometries allow the development of

numerical methods over years and provide a better understanding of the flow features around simplified car. Since the early 2010s, the international community has started working numerically on real cars, made possible by the increase of computer performances. In 2011, Heft et al. [19] made experiments and computations on a realistic car. The authors developed the DrivAer model, a mockup merged from the Audi A4 and the BMW 3 Series. They created a modular vehicle with 3 different shapes at the rear: Fastback, Notchback and Estate. Moreover, different configurations are possible, such as with or without side mirrors, front wheel spoiler, rear spoiler and realistic or simplified underbody. This model allows for the study of three different wakes on the same vehicle. For the Fastback and the Notchback configurations, flow separations are located around the trunk and the rear bumper, while for the Estate configuration, the flow massively separates on the rear of the vehicle. Complete experimental database are available for all these configurations. The reader can refer to Heft et al.[20], Strangfeld et al. [48], Avadiar et al. [7], Varney et al. [52] and Hupertz et al. [22].

From a numerical perspective, numerous studies have been conducted. Heft et al. ([19] and [21]) demonstrated that the SST RANS model provides good accuracy of 2 counts on the drag coefficient using the finest grid in their study, made of 20M cells. However, the near wall region was not resolved with $y^+ > 30$. The speed used in their study was not the typical 40 m/s used in automotive studies, but rather 16 m/s, which can influence the results due to Reynolds effects. Additionally, the authors investigated the methodology's robustness on several configurations, such as those with or without wheels and mirrors, and with smooth or detailed underbody. The simulation trends were inconsistent, sometimes under-predicting or overestimating the drag coefficient. The trend could stem from using a grid that is too coarse and fails to resolve turbulence close to the walls. Shinde et al. [39] studied a 2.5 scale reduction model. They computed the three DrivAer shapes with fixed and moving ground and with smooth and detailed underbody, using SST RANS model. The mesh was made of respectively 11M and 14M cells for smooth and detailed underbody with a $y^+ > 30$. The error prediction on drag is comprise between -2% and 12% with biggest mistake on the Estate configuration. However, the results should be interpreted with caution as the grid seems too coarse in the areas of interest to draw definitive conclusions on the results. Guilmineau et al. [17] worked on the Fastback configuration with a smooth underbody. They used the Explicit Algebraic Reynolds Stress Model (EARSM) and SST DES on two grids. Mesh 1 contained 19.3M cells with $y^+ = 6$ while Mesh 2 contained 38.7M cells with $y^+ = 0.3$, which means that the near wall region was resolved. Automatic grid refinement was then set into the wake during computation. Drag and lift coefficients were better predicted with DES. 3D results showed that there was no separation over the rear window, but there was a high intensity of the A-pillar vortices coming through the wake of the car. The pressure distribution on the top and bottom of the car showed good agreement for both turbulence models with experiments. Computations with grid refinement down to the wall showed interesting and robust results compared to previous studies. Ashton et al. [6] conducted a study on the Fastback and Estate configurations. In this complete study, five grids were created, all resolving the near-wall with $y^+ < 1$. Three grids were made for RANS simulations, with 18M (coarse), 37M (medium) and 80M (fine) cells. For DDES, two grids were made of 80M (coarse) and 100M (fine) cells. The following turbulence models were compared: SA, SST, RKE, RSM, SA DDES, SA IDDES and SST IDDES. Aerodynamic coefficients were compared for RANS on the finest grid (80M) and for hybrid RANS/LES on both coarse (80M) and fine (100M) grids. RANS simulations, especially SA and SST, provided good agreement for drag prediction in the Fastback case. However, lift was poorly computed for all RANS models, as observed in the previous detailed studies. For Estate, the results were worse with RANS compared to Fastback. This confirms the complex challenge of predicting the Estate flow features with massive separation in the wake. Then, the results showed that all hybrid RANS/LES results (regardless of mesh resolution or DES variant) provide better predictions on drag and lift coefficients compared to RANS simulations. Flow characteristics for both vehicle configurations are also more accurately predicted with RANS/LES methods. A detailed 3D study of the wake showed that the RANS model predicts a lower value of Turbulent Kinetic Energy (TKE) than any of the DES variants. Reduced levels of TKE would result in lower levels of turbulent mixing, and as a consequence, a greater recirculation region. With DES variants, the correct level of TKE ensures accurate predictions of the separation in the wake, leading to a global accurate prediction on the whole wake. In more recent years, LES studies have been carried out on DrivAer models. Rüttgers et al. [37] studied the Fastback DrivAer model, with smooth underbody and rotating wheels. The authors made a Wall-Resolved LES based on a convergence grid study made of three grids with respectively 24, 80 and 130 million cells. A $y^+ < 2$ was used to resolve the near-wall region, however only 5 prism layers were generated with a growth ratio of 1.5 which seems not enough to fully resolved the boundary layer for WRLES. The finest grid showed the best result on drag prediction compared to experiments. A discrepancy of 15 counts was computed, i.e a 6.2% error. Menter et al. [31] computed a Wall-Function LES on the Notchback DrivAer using GPU solver over two grids made of 250 and 500 million cells. The use of wall function allowed the authors to use a grid with $y^+ > 30$ and then focused on wake resolution rather than boundary layer resolution. The LES results were compared to SBES computation made for AutoCFD2 Prediction Workshop. The drag prediction for SBES, 250M LES and 500M LES was respectively of 24 counts, 10 counts and 2 counts (1% error). The 500M LES showed very good agreement with experiments in the underbody area compared to SBES while the wake prediction was globally the same between the two methods. LES with wall functions showed encouraging results for the near future. Similar study over Estate or SUV shape will be of major interest.

Others studies, not detailed here, can be interesting for the reader: Fotiadis et al. [15], Peters et al. [34], Wang et al. [54] and Wieser et al. [56].

To summarize, studies on the Fastback and Notchback configurations have shown that RANS can predict the flow features and aerodynamics forces with correct accuracy when the grid is fine enough down to the wall. For these configurations, hybrid RANS/LES is not mandatory to accurately reproduce the flow features. In contrast, for the Estate case, hybrid RANS/LES is required to accurately predict the wake of the car, as well as the drag and lift coefficients. Finally, probably due to its flow complexity and the requirement for grid refinement, the Estate configuration seems to have been less studied numerically compared to the two others shapes in the literature.

This work follows the previous publication by the authors [12] where the authors fine-tuned a numerical procedure for external aerodynamics flow predictions, based on Ahmed bodies. Several RANS and hybrid RANS/LES methods were compared to conclude that, with the given grid and numerical setup used, DDES was the best model on Ahmed bodies. The aim of this paper is to apply the same numerical methodology to a realistic Estate shape and explore the superiority of hybrid RANS/LES method over steady computations with RANS. Accurately simulating the flow dynamics around such a complex geometry requires a careful computational methodology. Therefore, transitioning to unsteady numerical method is necessary to accurately capture the flow features. This paper includes a detailed analysis of the flow around the car, particularly in the wake region. The focus on the near wake is crucial, as a significant portion of the drag forces are due to the flow topology in the rear part of the vehicle.

This paper is structured as follows. Sect. 2 presents the geometries studied, the Ahmed body and the Peugeot Estate car. Sect. 3 provides details on the experimental measurements carried out in S2A Wind Tunnel. Sect. 4 outlines the computational setup, including turbulence models and numerical setup used in this study. Since this work follows the DDES calibration method done by the authors, previous results on Ahmed body are summarized in Sect. 5. Sect. 6 and Sect. 7 respectively compare numerical results on the Peugeot Estate car based on grid convergence study and then, on the comparison of 2D and 3D results between turbulence models and experiments. Finally Sect. 8 provides the main conclusions of this work and suggestions for further research.

2 Geometries presentation

The Ahmed body [2] with sharp edges is a very simplified car, made of a forebody, a long mid-section assumed to suppress interactions between the front and the back of the body and a variable rear slant angle. It reproduces some of the flow features visible on a real vehicle, such as the 3D recirculation in the wake of the body and the longitudinal vortices. The longitudinal vortices are found around the front window edges (A-pillar vortices) and at the back of notchback shape vehicle (C-pillar vortices) for instance. The most challenging case for computational simulation around Ahmed body is the one with a rear slant angle of 25°. The 25° Ahmed body was selected to develop the methodology used in [12]. Geometric description of this body is pr

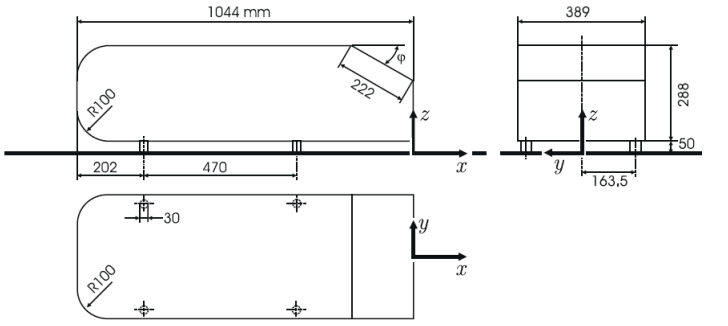

(a) schematic representation

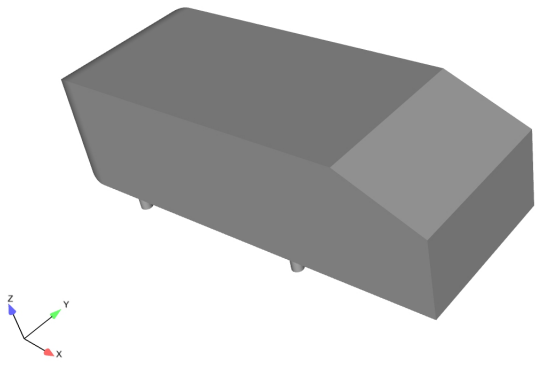

(b) rear view of the 25° Ahmed body

Fig. 1: Geometric representation of the 25° Ahmed body.

To move forward from the simplified Ahmed body geometry, a realistic geometry of a real vehicle is introduced here. The vehicle is the 2013 Peugeot 308 SW (Station Wagon). The car is represented in Fig. 2. In order to avoid a

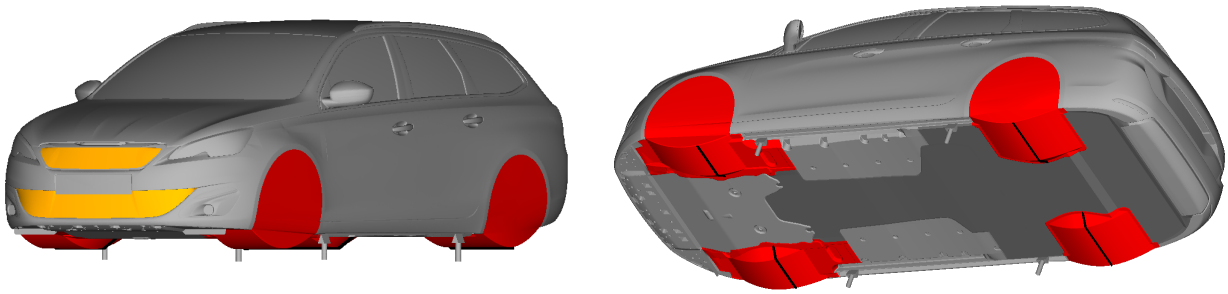

(a) isometric view of the 308 SW

(b) underbody view of the 308 SW

Fig. 2: Geometric representation of the simplified vehicle.

huge step from the simplified Ahmed body to a fully realistic production car, and to validate the numerical methodology step by step, some simplifications on the vehicle have been done:

- the front air inlets are closed (orange color), meaning there is no airflow in the underhood area
- the underbody is smoothed with additional panels (dark gray color)
- the wheels are removed, replaced by fairings (red color) with small spoiler (black color) to force the flow to separate at their locations.

Moreover, the struts of the wind tunnel to fix the car are represented into the numerical geometry. The length, width, and height of the Ahmed body are respectively $L_{AB} = 1044$ mm, $W_{AB} = 380$ mm and $H_{AB} = 288$ mm with AB stands for Ahmed Body abbreviation. The same dimensions for the car are respectively $L_V = 4585$ mm, $W_V = 1804$ mm and $H_V = 1471$ mm with V stands for Vehicle abbreviation. The vehicle is 4-5 time bigger than the Ahmed body.

3 Experiments

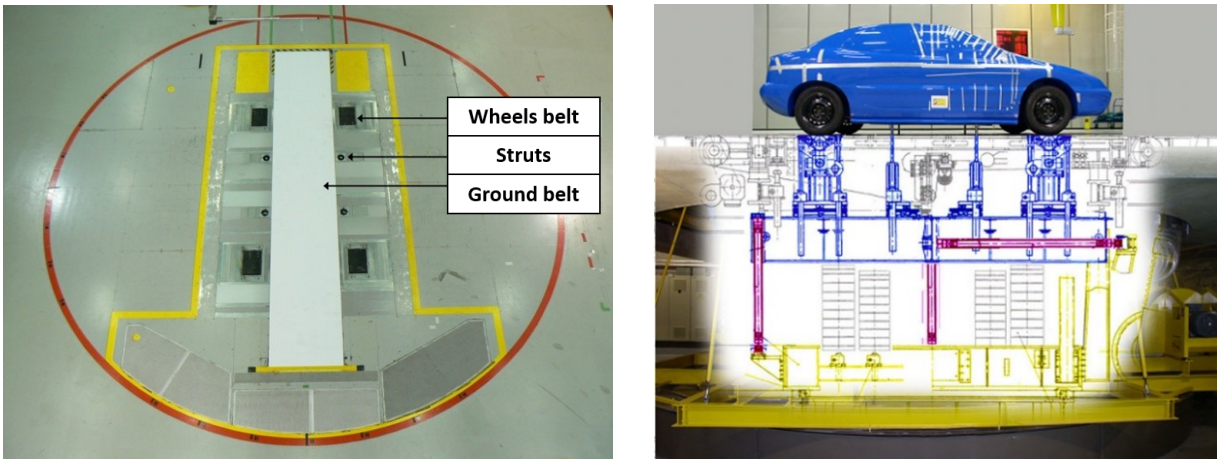

(a) 4 belts for the wheel and 1 for the ground

(b) Weighing system sketch

Fig. 3: Illustration of S2A wind tunnel [49].

Experiments have been carried out in the S2A full-scale automotive wind tunnel, in France [49]. The open return wind tunnel consists of an $3/4$ open jet test section with an 24 m^2 nozzle, with respectively width and height of 6.5m and 3.7m. Wind speed can vary from 0 to 240kph. In these experiments, the reference velocity is set to 140kph. When tomographies are done, the velocity has to be reduced to 120kph. Fig. 3 (a) is a top view where the car is setup in the nozzle. The rolling road is simulated using the ground belt, which is 6m long and 1m width. 4 belts are used for the wheels. Each belt can reach the speed of 200 kph. The car is fixed using 4 struts illustrated on the picture. In

(a) C_p probes on the rear window

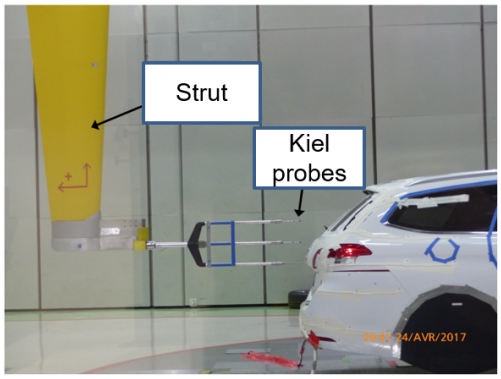

(b) tomography measurement

Fig. 4: Illustrations of C_p probes position and tomography measurement.

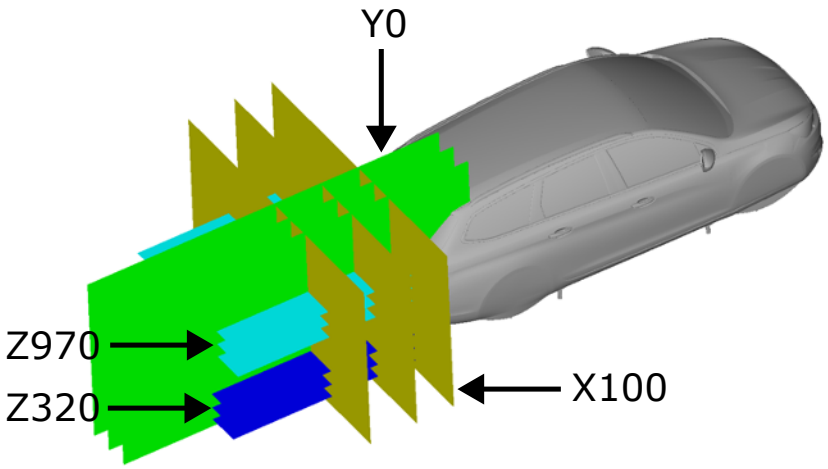

Fig. 5: Illustrations of all measured planes using tomographies.

the presented experiments, due to the wheels removal, the belts are fixed (stationary mode activated). The red circle delimits the rotating cylinder, which is used to mimic yaw angle wind. Fig. 3 (b) presents a sketch of the weighting system. The 6 components aerodynamic loads are measured from the 4 struts and the 4 wheels belts. Drag (C_d) and lift (C_l) coefficients have respectively a precision of 0.002 and 0.03 [55], corresponding to a measurement error of 0.3% and 3.5% on C_d and C_l. Each configuration has been repeated twice, to ensure the accuracy of the measured results. Moreover, the control of the boundary layer around the vehicle is controlled with two areas of boundary layers suction: one at the exit of the convergent and one just before the ground belt. The Peugeot Estate vehicle presented on Fig. 2 is a full-scale car. All of the detailed geometric modifications were realized on the production vehicle in order to carry out full scale measurements into the wind tunnel. To validate the geometric accuracy of the physical model in the underbody, the final product has been scanned and used as the reference numerical geometry. During this experimental campaign, a huge database was set up: drag and lift coefficients, parietal pressure coefficient (C_p) using pressure probes, oil visualization on the rear to detect flow separation, 2D PIV (Particle Image Velocimetry) and tomographies in the wake of the vehicle. Fig. 4 (a) shows the position of the pressure probes on the rear of the car. A total of 90 probes were set up around the vehicle. Fig. 4 (b) depicts the tomography setup. Three Kiel probes are mounted on a NACA strut that moves behind the vehicle. Each probe is an omnidirectional 18 holes probe and is therefore capable of measuring pressures and velocities in both, direct and reverse complex flows. This is suitable to measure the flow in the wake of a car. Moreover, it is an easiest and fastest way to have 3D data compare to PIV, due to the tedious preparing time to setup laser and cameras at the perfect location around the car. The spacing resolution is a 10x10 mm grid in the measured plane. Fig. 5 presents all the measured planes: 3 yellow planes in X axis (X100, X500 et X1000 mm behind the car, assuming that the longitudinal extremity of the car is for X=0 mm), 3 green planes in the Y axis (Y0, Y250 and Y500 mm, with Y0 the symmetry plane of the car), 3 blue planes in the Z axis (Z170, Z320 and Z470 mm from the ground, assuming that Z=0 mm is the ground position - lower part of the wake) and 3 cyan planes in the Z axis (Z820, Z970 and Z1120 mm from the ground - upper part of the wake). For the correlation between computations and experiments, Y0, Y500, X100, Z320 and Z970 planes will be use in Sect. 6 and Sect. 7.

4 Computational setup

4.1 Numerical method

The CFD simulation results presented in this study have been carried out with ANSYS Fluent 2020R2 CFD code [4]. It uses a 3D finite volume method with a cell-centered data arrangement to solve the incompressible Navier-Stokes equations. ANSYS uses a control-volume-based technique to convert a general scalar transport equation to an algebraic equation that can be solved numerically. The computational domain is divided into discrete control volumes, known as cells. The transport equation is integrated on each control volume, yielding a discrete equation that expresses the conservation law on a control-volume basis. For a matter of simplicity, let us consider the integral form of the unsteady conservation equation for the transport of a scalar quantity Φ on an arbitrary volume control V. The equation is as follows:

$$\int_V \frac{\partial \rho \Phi}{\partial t} dV + \oint \rho \Phi \overrightarrow{v}.d\overrightarrow{A} = \oint \Gamma_\Phi \nabla \Phi.d\overrightarrow{A} + \int_V S_\Phi dV \tag{1}$$

where ρ, $\overrightarrow{v}$, $\overrightarrow{A}$, Γ_Φ, $\nabla\Phi$ and S_Φ are respectively the fluid density, the vector velocity, the surface area vector, the diffusion coefficient for Φ, the gradient of Φ and the source term of Φ per unit volume. Discretization of Equation (1) on a control volume yields:

$$\frac{\partial \rho \Phi}{\partial t} V + \sum_f^{N_{faces}} \rho_f \overrightarrow{v_f} \Phi_f . \overrightarrow{A_f} = \sum_f^{N_{faces}} \Gamma_\Phi \nabla \Phi_f . \overrightarrow{A_f} + S_\Phi V \tag{2}$$

where N_{faces}, Φ_f, $\rho_f \overrightarrow{v_f}.\overrightarrow{A_f}$, $\overrightarrow{A_f}$, $\nabla\Phi_f$ and V are respectively the number of faces enclosing the current cell, the value of Φ convected through face f, the mass flux through the face, the area vector of face f, the gradient of Φ at face f and the cell volume. The discretized Equation (2) contains the unknown scalar variable Φ at the cell center and the unknown values in surrounding neighbor cells. This equation is nonlinear with respect to these variables. A linearized form of Equation (2) can be written as

$$a_P \Phi = \sum_{nb} a_{nb} \Phi_{nb} + b \tag{3}$$

where nb refers to neighbor cells, a_P and a_{nb} are the linearized coefficients for Φ and Φ_{nb}. The numbers of neighbor for each cells depend on the grid topology and equal the number of faces enclosing the cell. Similar equation can be written for each cell of the grid. This results in a set of algebraic equations. ANSYS Fluent solves this linear system using a point implicit Gauss-Seidel linear equation solver coupled with an algebraic multigrid method. This procedure is then applied to the steady-state continuity and momentum equations in integral form as follows:

$$\oint \rho \overrightarrow{v}.d\overrightarrow{A} = 0 \tag{4}$$

$$\oint \rho \overrightarrow{v}\overrightarrow{v}.d\overrightarrow{A} = -\oint pI.d\overrightarrow{A} + \oint \overline{\overline{\tau}}.d\overrightarrow{A} + \int_V \overrightarrow{F} dV \tag{5}$$

where I is the identity matrix, $\overline{\overline{\tau}}$ is the viscous stress tensor and $\overrightarrow{F}$ is the force vector.

There are 3 different ways to solve numerically the Navier-Stokes equations detailed above. The first one is Direct Numerical Simulation (DNS) which consists of the resolution both in space and time of all the turbulent spectrum. Moreover, very small time step and non dissipative schemes are required to capture all turbulent structures without artificially damping them. However, for a high Reynolds number application such that the external flow around a detailed vehicle, the numerical cost is prohibitive with the current resources available. The opposite trend is the Reynolds Averaged Navier-Stokes (RANS) equations. By introducing the Reynolds decomposition, i.e the velocity field can be decomposed with an average velocity and a fluctuation velocity around the average one, the RANS equations are obtained. RANS equations model all the turbulent scales using a closure model. The advantages of RANS models are the low computational cost and convergence robustness due to the averaged equations. However, due to the modeling aspect of this model, mean flows can be rather wrong compared to experiments. The third approach, the Large Eddy Simulation (LES) is located between RANS and DNS resolution, regarding flow resolution and therefore numerical cost. A large part of the energy spectrum is resolved, while the smaller scales compared to the grid size (usually identified as the dissipation range in the turbulent spectrum) are modeled using sub-grid scale models or the use of the truncation error of high order numerical scheme to mimic a sub-grid model. The latest method is known as Implicit LES ([1], [14]). When the near-wall region is fully resolved, LES is named Wall-Resolved LES (WRLES). However, due to high grid spacing requirement, WRLES is currently not achievable for a high turbulent flow around a full scale car. To make LES affordable, other techniques have been developed other years. Wall-Modeled LES (WMLES) model ([35], [40])

uses a RANS model only in the innermost part of the wall boundary layer and then switch to a LES model for the main part of the boundary layer. Wall-Functions LES (WFLES) model ([8], [24]) allows the resolution of a boundary layer volume using a constant number of cells, independent of the Reynolds number. In practice, the first cell node is placed as $y^+ > 30$. These two models allow a significant reduction of grid point required in the boundary layer compared to WRLES. Other approaches named Zonal LES [10] and Embedded LES [36] can be used when the user wants to define the RANS and the LES regions a priori of the computation. More recently, hybrid RANS/LES approaches were developed to take advantages from both RANS and LES formulations. RANS is then used in the boundary layer where LES requires non affordable fine grid. When separation is detected, the model switches to LES mode in order to resolve as much scales as possible, based on grid refinement. At the moment, hybrid RANS/LES methods are the most advanced methods that can be used regarding the CPU performances in industrial High-Performance Computing (HPC) environment. Spalart [44] suggested that WRLES and DNS would be available respectively in 2050 and 2080 for a full scale geometry at high Reynolds number. However, revolution in HPC could arrive ahead of schedule. Indeed, GPU solvers are now released from commercial code editors and enhance the computing performances. Faster simulations can be obtained and/or the possibility to increase the grid refinement beyond a new level. A detailed study made on a realistic aircraft model in landing configuration by Goc et al. [16] compared both CPU and GPU performances over WMLES simulations. With 2000 CPU cores and 96 GPU, the wall-clock time to 30 flow passes is respectively of 7.5 days for CPU and 7 hours for GPU on 157 million cells. This study shows tremendous improvements on computational time reduction with GPU. The next step will probably be the quantum computer that would be able to operate 100 trillion times faster than any supercomputer. However, the feasibility with such quantum computer has to be explored and confirmed in the future.

In this paper, two eddy viscosity RANS models, RKE and SST, are used and compared to SST DDES hybrid RANS/LES models. The three turbulence models are detailed in the following sections.

4.1.1 RKE RANS model

The Realizable $k-\varepsilon$ (RKE) model developed by Shih et al. [38] is an evolution of the Standard $k-\varepsilon$ (SKE) model [25]. This model consists of two main changes compared to SKE model:

- a new model dissipation rate equation based on the dynamic equation of the mean-square vorticity fluctuation for large Reynolds number
- a new realizable eddy viscosity formulation based on the positivity of square Reynolds stresses and Schwarz' inequality for turbulent shear stresses

The RKE model has shown significant improvement on many flow applications compared to SKE model [38]. For this reason, RKE model is widely use in industrial application for its robustness and its low cost computation. The main drawback of this model is the underestimation of Turbulent Kinetic Energy (TKE or k) level in separation area. It results to overestimation of recirculation length in most of the cases.

As the ε equation is not derivable down to the wall, wall function is required. In this work, the Enhanced Wall Treatment (EWT) from ANSYS Fluent is used. This is a 2-layers formulation. In this approach, the whole domain is subdivided into a viscosity-affected region and a fully-turbulent region. The demarcation of the two regions is determined by a wall-distance-based, turbulent Reynolds number Re_y, defined as $Re_y = \frac{\rho.y.\sqrt{k}}{\mu}$, with y the wall-normal distance calculated at the cell centers. The demarcation between the two areas is made at $Re_y = 200$. When Re_y is lower than 200, near to the wall, the one-equation model of Wolfstein [57] is employed to compute the turbulent viscosity. When Re_y is larger than 200, the $k-\varepsilon$ formulation is employed.

The RKE EWT is used as the numerical reference for external flow application in this work.

4.1.2 SST RANS model

SST RANS model is known as one of the more accurate turbulence model for separation prediction compared to $k-\varepsilon$ and $k-\omega$ formulations. SST model combines the strengths of $k-\omega$ in the boundary layer and gradually switches to a $k-\varepsilon$ formulation in the outer part of the boundary layer to liberate from freestream dependency of the $k-\omega$ model [27]. The blending between $k-\varepsilon$ and $k-\omega$ formulations is ensured with the F1 blending function. This model is sensitized to adverse pressure gradient by taking into account the shear stress transport, modifying the eddy viscosity formulation in the boundary layer of the model, with the blending function F2. The reader can found more details on the construction of the model in the original paper of Menter [28].

Unlike the ε equation, the ω equation can be integrated through the viscous sublayer without the need for a two-layer approach. This feature can be utilized for a y^+-insensitive wall treatment by blending the viscous sublayer formulation ($w^+_{sub} = \frac{6}{C_{\omega 2} y^{+2}}$) and the logarithmic layer formulation ($w^+_{log} = \frac{1}{\sqrt{C_\mu} y^+}$) based on y^+, with $C_{\omega 2}$ and C_μ constants from

$k-\omega$ model. Therefore, SST model requires the first node of the mesh to be in the viscous sublayer as $y^+ \simeq 1$. This feature of the model is respected in the build process of the grids detailed in Sect. 4.4.

4.1.3 Delayed/Detached Eddy Simulation models - DES/DDES

In 1997, Spalart et al. [43] proposed an hybrid RANS/LES formulation, the so-called Detached Eddy Simulation or DES97. The main purpose of this model is to use the strong points of both RANS and LES computation in different parts of the flow in order to reduce the computational cost without losing accuracy compared to LES simulations. The grid refinement is prohibitive in the near wall region (attached boundary layer) for LES computation, so that, in this flow area, DES97 model will act as RANS model. In massively separated regions, RANS models are known to suffer from inaccurate prediction of flow separation and recirculation length. As a consequence, in order to resolve as much as possible scales, LES is activated in this flow area. To achieve this blending between RANS and LES formulations, the dissipation term in the k equation of the SST RANS model is modified as follows [50]:

$$Y_k = \rho\beta^* k\omega => Y_k = \rho\beta^* \frac{k^{3/2}}{l_{DES}} \tag{6}$$

with β^* a function of the SST RANS model detailed in [50] and l_{DES} the modified length scale of the DES model defined as

$$l_{DES} = min(l_{RANS}, l_{LES}) \tag{7}$$

$$l_{RANS} = \frac{\sqrt{k}}{\beta^*\omega} \tag{8}$$

$$l_{LES} = C_{DES}\,\Delta_{max} \tag{9}$$

With Δ_{max} the maximum local grid spacing defined as $\Delta_{max} = max(\Delta_x, \Delta_y, \Delta_z)$ and $C_{DES} = C_{DES1}.F_1 + C_{DES2}.(1-F_1)$ with $C_{DES1} = 0.78$ and $C_{DES2} = 0.61$.

The switch between RANS and LES occurs when $\Delta_{max} < \delta$ with δ the boundary layer thickness. In a boundary layer, Δ_{max} is lead by the streamwise (x) and spanwise (y) resolution of the wall, as the vertical direction (z) is refined a lot compared to the two others directions, so $\Delta_{max} = max(\Delta_x, \Delta_y)$. Violating this criterion can lead to destruction of the numerical simulation. Menter and Kuntz [29] faced Grid-Induced Separation (GIS) due to high grid refinement in the boundary layer. This phenomenon has been renamed by Spalart et al. [46] as Modeled-Stress Depletion (MSD). MSD happens when LES penetrates the upper part of the boundary layer where the grid is not fine enough to resolve the velocity fluctuations. Then, the model reduced the eddy viscosity, leading to transfer from modeled stress to resolved stress while the grid cannot sustain LES resolution. In this context, GIS happens. In reality, GIS is a consequence of MSD. Moreover, a classical problem appears for all hybrid RANS-LES methods and was identified in the DES97 publication [43]: the gray area. It corresponds to flow area where the transition between RANS and LES is occurring. In this area, the initial lack of resolved turbulence results in neither RANS nor LES resolution.

The reader is referred to Mockett PhD work [33] for more details on DES.

Spalart et al. [46] improved the protection of the boundary layer, yielding to the Delayed DES model (DDES). For DDES model, the shielding function takes into account both the distance to the wall and eddy-viscosity field, which is time-dependent. The delay function f_d is defined as follows by Spalart et al. [46]:

$$f_d = 1 - tanh\left[(Cd_1 r_d)^{Cd_2}\right] \tag{10}$$

The r_d parameter represents the ratio of a model length scale to the wall distance. The f_d function is designed to be equal to 1 in LES region, where $r_d \ll 1$, and 0 elsewhere when $r_d > 1$. The constants Cd_1 and Cd_2 are respectively 20 and 3 to ensure a fair protection of boundary layer with SST model [18]. The DDES length scale reads as follows:

$$l_{DDES} = l_{RANS} - f_d\, max(0, l_{RANS} - l_{LES}) \tag{11}$$

This new formulation of the shielding function ensures a stronger protection of the boundary layer from LES intrusion. Menter [26] defines the ratio $r = \frac{\Delta_{max}}{\delta}$ and shows that the impact of grid refinement is delayed to $r < 0.2$ in DDES, compared to $r < 1$ in DES. It shows the GIS phenomenon is strongly reduced with this new formulation of the model. Moreover, the gray area is reduced due to faster transition from RANS to LES [46].

It can be shown under the assumption of local equilibrium (i.e. equality of the generation and dissipation terms of the transport equations) that DDES sub-grid scale model reduces to Smagorinsky-Lilly model [42].

4.2 Numerical schemes and time step

Convective fluxes are approximated with the second order Bounded Central Differencing (BCD) scheme [23], which consists of a blend between pure central difference scheme, second-order upwind scheme and first-order upwind scheme. Diffusive terms are discretized with second order central difference scheme. The pressure values at the faces are discretized using second order central differencing scheme. Gradients are computed using the average of the nodal values on the considered face. The SIMPLEC algorithm is used for pressure/velocity coupling. The temporal resolution is achieved with second order implicit scheme, ensuring the numerical scheme to be unconditionally stable. For hybrid RANS/LES methods, as in LES computations, low dissipation schemes are required to allow the resolution of the resolved 3D scales. Classical second order upwind scheme would annihilate the turbulent structures in the flow. On the contrary, pure Central Differencing (CD) scheme can be unstable or produce nonphysical wiggles in the solution. Even if BCD scheme is slightly more dissipative than CD scheme, it is the optimal choice.

In computational simulations, the time step can be related to a non dimensional number, the Courant-Friedrichs-Lewy (CFL) number. This number is defined as $CFL = \frac{V_\infty \Delta t}{\Delta x}$ with V_∞ the free stream velocity, Δt the time step and Δx the grid spacing. Generally, especially for explicit time integration, a CFL lower than one is required for scheme stability. In practice, even with the use of implicit time integration, which is unconditionally stable, a CFL close to one is also advised. The $CFL < 1$ can be viewed as follows: a flow particle should not cross more than one cell during one time step. Beyond, flow information can be canceled. For this reason, a careful attention on the grid and the time step is required to avoid the damping or vanishing of turbulent structures. From our experience and previous works, we advised a maximum value of 5 for the CFL number in the LES region. With higher values, turbulent structures can be badly computed or even vanished. In this work, a time step ramp method is used to increase the convergence speed of the computations. The initial time step is 10 times larger than the final time step defined as $\Delta t = 5 \times 10^{-5}$s, ensuring a CFL number below 2 around the car. The corresponding non-dimensional time step is defined as follows $\Delta t.V_\infty/L_v = 0.00044$. The computations were run for a total of 27 convective transit times defined as $T.V_\infty/L_v$, with $T = 3$ seconds of physical time. The ramp method is only used on the first second of the computation. The time-averaging process was started after 14 transit times (1.5 seconds of physical time), ensuring the relevance of the averaged quantities during 1.5 seconds. In addition, all of the post-processed variables in the below sections (C_d, C_l, C_p, V_x, V_y, V_z, Ω_x and Ω_y) are time-averaged.

4.3 Domain setup

The computational domain, schematized in Fig. 6, is respectively $3L_v$ long upstream the car and $5L_v$ long downstream the car, with L_v the length of the vehicle. The cross width of the domain is equal to $4L_v$ and its height is set to $3L_v$. The blockage ratio is computed as the ratio between the frontal area of the body over the inlet section of the numerical wind tunnel. It gives a blockage ratio of $0,5\%$. The inlet boundary condition is defined as velocity inlet with $V_\infty = 140\ kph$, leading to a Reynolds number based on the length of the body Re_L equal to 1.3×10^7. Turbulent quantities at the inlet are set with the viscosity ratio ν_t/ν, defined as the ratio of turbulent viscosity ratio ν_t over the kinematic viscosity ν of the air, equal to 10 and the turbulent intensity I set to 0.5% as in experiments. A pressure outlet condition is applied to the exit surface, with gauge pressure equal to 0 Pa. No-slip wall boundary conditions have been applied on the body based on the integration of the governing equations down to the wall itself. The same boundary conditions are used on the sides and the roof of the computational domain. The use of no-slip wall condition is possible as the blockage ratio is very low and it has no influence on the global flow. The experimental air density, based on a nozzle temperature of 20°, is reproduced in computation with $\rho = 1.204\ kg/m^3$ and the corresponding kinematic viscosity $\nu = 1.7894\ \times 10^{-5} kg/m.s$. From wind tunnel experiments, the boundary layer thickness is equal to 65 mm in the center of the wind tunnel without any body. To reproduce the experimental boundary layer thickness, the ground of the computational domain is divided into two parts: from the inlet to $X/L_v = -1.5$, a slip wall condition is applied and the remainder part of the ground is defined as a no-slip wall condition to allow the build up of the boundary layer. This is the simplest way to reproduce experimental boundary layer thickness. For starting the computation from scratch, the whole numerical domain is initialized with zero velocity. Then, the flow enters the domain by the inlet with a constant entrance velocity and turbulent conditions defined above.

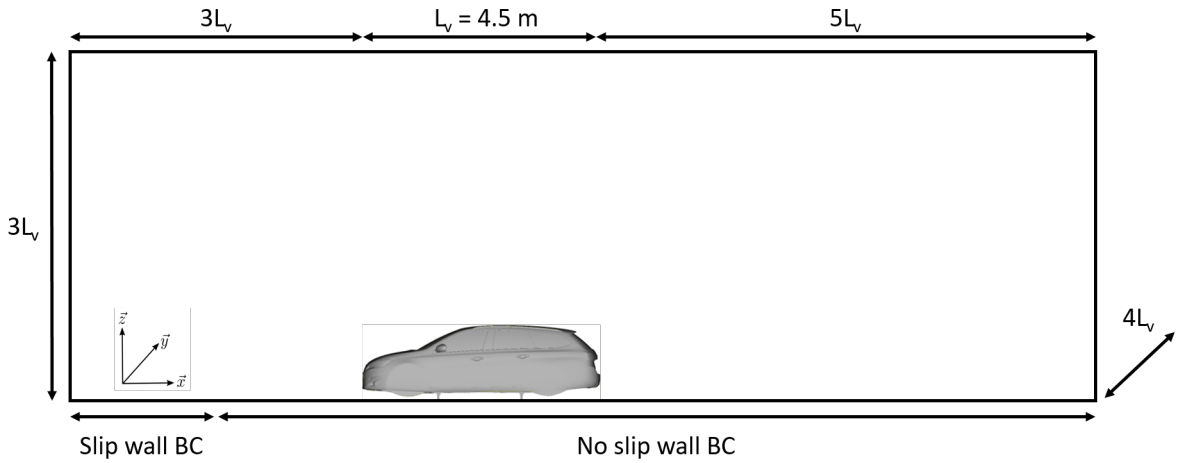

Fig. 6: Schematic representation of the computational domain.

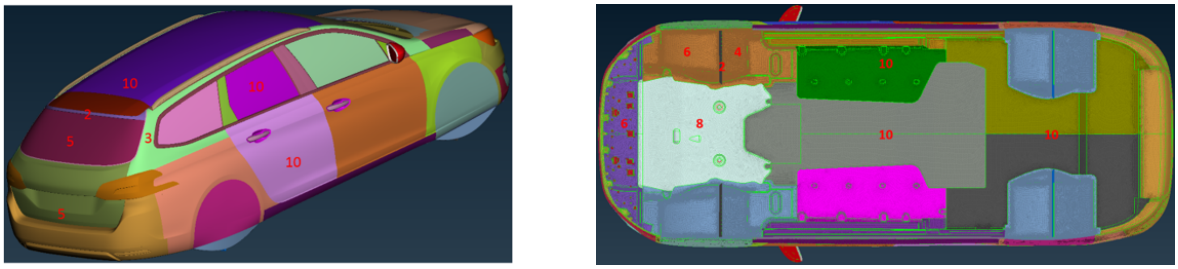

(a) 2D mesh on the body superstructure

(b) 2D mesh on the underbody

Fig. 7: 2D mesh size on the vehicle.

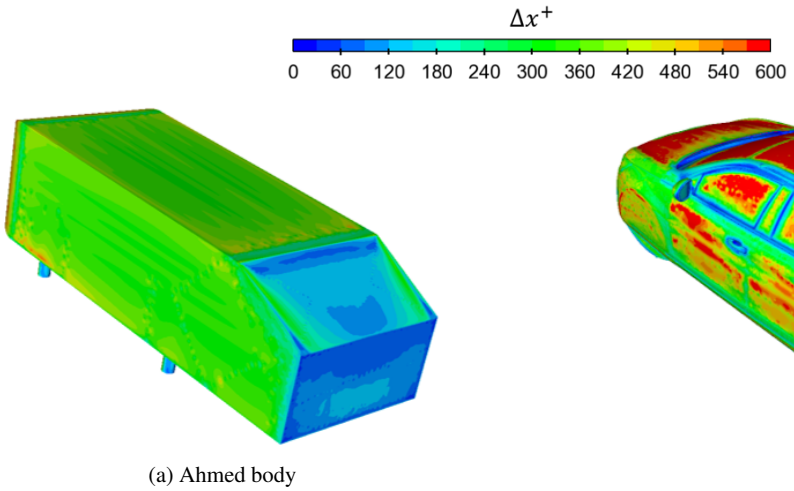

(a) Ahmed body

(b) Vehicle

Fig. 8: Δx^+ evolution on Ahmed body and vehicle geometries.

4.4 Grids

The 2D mesh size, made of triangles, is presented in Fig. 7. The same 2D mesh is used for all grids presented below. The grid refinement is based on Stellantis' experience and grid study realized during this work and the previous one [12]. The size of the cells are set to 2 mm (around sharp edges as windows pillar, spoiler and mirror screens) to 10 mm on flat areas (bonnet, roof, sides, underbody). The rear window and the back of the vehicle are meshed in 5 mm. The transition from the sides and the rear window is meshed in 3 mm in order to well capture the flow separation. The underbody is smoothly less refined from 6 mm for the engine belly pan to 10 mm at the end. The fairings are meshed

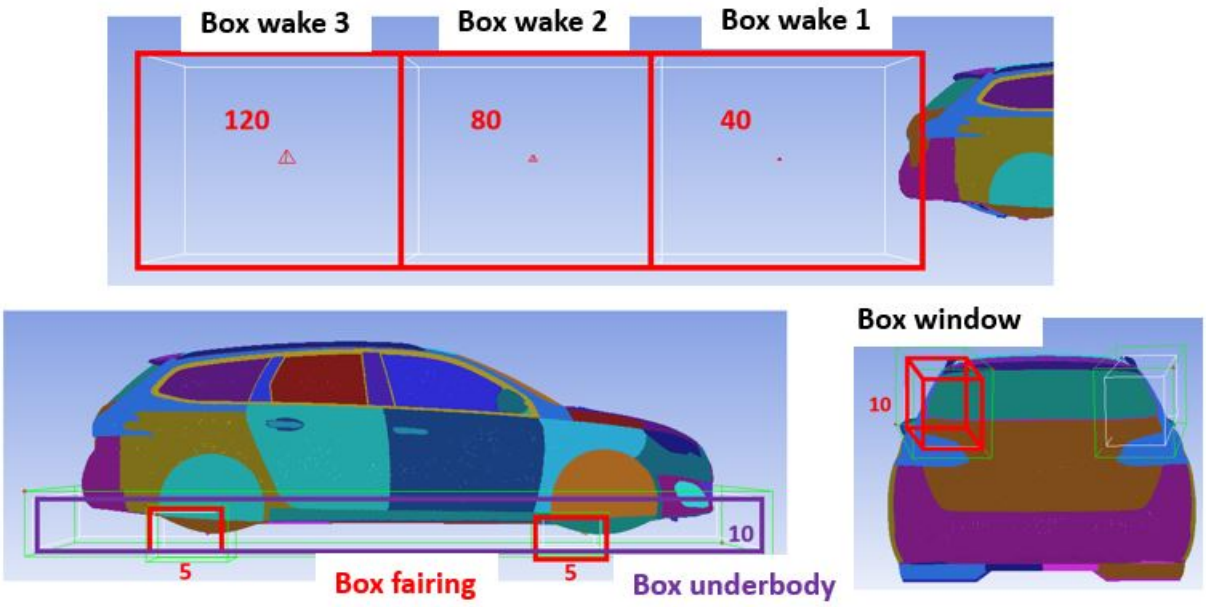

Fig. 9: Reference grid - 115M elements.

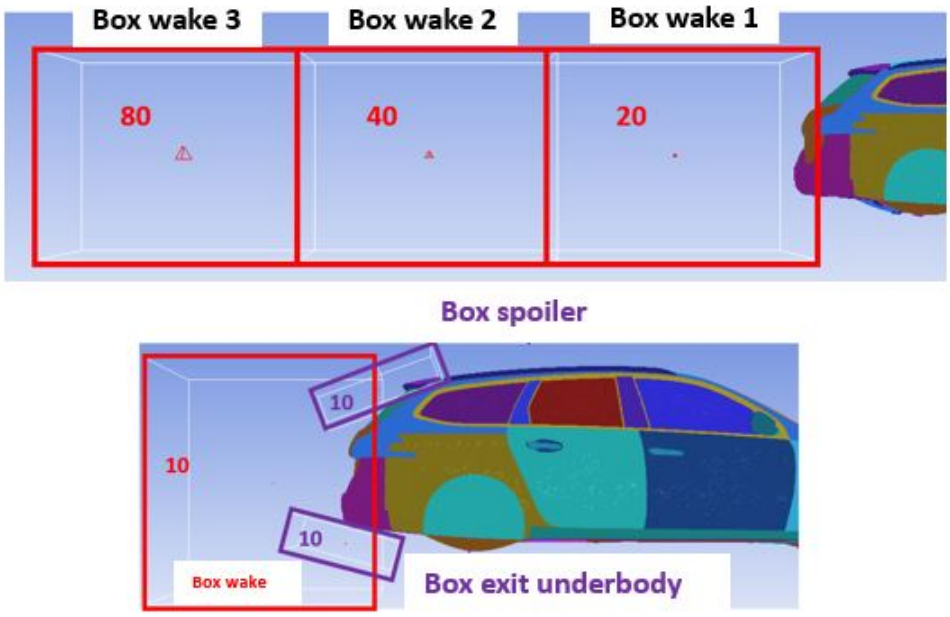

Fig. 10: Refined grid - 185M elements.

in 6 mm and 4 mm respectively downstream and upstream the separation area, marked by the small spoiler meshed in 2 mm.

Fig. 8 presents the evolution of normalized size of the mesh with Δx^+ on the Ahmed body and the vehicle. Δx^+ is defined as $\Delta x^+ = \frac{u_\tau \times \Delta x}{\nu}$ with u_τ, Δx and ν are respectively the friction velocity, the grid spacing in the longitudinal direction and the cinematic viscosity of the fluid. As 2D triangles are used, longitudinal and spanwise normalized values are identical. On the roof, approximate values of 300 and 600 are observed respectively for the Ahmed body (2D mesh = 4 mm) and the vehicle (10 mm). On the rear, these values are respectively around 120 for the Ahmed body (2D mesh = 3 mm) et 70 for the vehicle (5 mm). These values show that the grid is less refined on large flat area on the vehicle compared to Ahmed body, in order to respect the Menter's criterion and avoid LES intrusion inside the boundary layer with DDES model. On the contrary, on the back, in the separation area, the grid is almost as fine as the Ahmed body mesh.

	BW	BW 1	BW 2	BW 3	UB	Exit UB	Fairings	Spoiler	Window
Reference	20	40	80	120	10	10	5	20	20
Refined	10	20	40	80	10	5	5	10	10

Table 1: Comparisons of 3D grid size in mm around the vehicle for the Reference and Refined grids. BW and UB respectively stand for Box wake and Underbody parts of the vehicle.

Based on the work realized on the Ahmed body [12], grids with 20 and 30 prism layers have been realized on the vehicle. Moreover, the rise of Cd_1 constant of the DDES model from 20 (default value) to 30 has been investigated as well. With the value of 30, the shielding of the boundary layer is increased, as observed on the Ahmed body case, and then advised for this case.

The 20 prism layers are created using a uniform algorithm with geometric expansion. The first height h_1 is equal to 0.020 mm with a grow ratio of 1.4 between each layer. With these parameters, the whole boundary layer is enclosed into the prism cells (16 mm on the Ahmed body and 45 mm on the vehicle). This setup leads to y^+ value around 1 on the vehicle, as recommended for SST turbulence models. The 30 prism layers keep the h_1 value from the 20 prism layers grid as the y^+ value is around 1. The total height is also kept constant. It means that the grow ratio is reduced from 1.4 to 1.23. This value is consistent with the value advised by Spalart et al. [45], where growth ratio for hybrid method should be inferior to 1.25.
The rest of the computational domain is filled with tetrahedron cells. The user has to give to Fluent Meshing a targeted volume size. For matter of simplicity, we are using a reference length L_{ref} defined in mm. This length corresponds to the edge size of a perfect tetrahedron, where the volume is defined by $V = L_{ref}^3 * \sqrt{2}/12$. A total of 8 refinement boxes is used to refine the grid in strategic locations around the vehicle. The locations of the boxes are depicted on Fig. 9 and Fig. 10, respectively for the Reference grid and the Refined grid, and detailed as follows:

- Wake - 4 boxes: a global wake refinement, from direct vicinity of the car *Box wake* to further location in the wake, corresponding to two length car behind the vehicle *Box wake 3*.
- Underbody - 3 boxes: *Box underbody* all along the underbody, *Box exit underbody* to capture the shear layer at the rear separation and *Box fairing* to capture separation around fairings.
- Rear window - 2 boxes: *Box window* and *Box spoiler* to capture the flow separation around the rear window.

Tab. 1 gives an overview of the grid sizes in the 8 refinement boxes for the two studied grids, Reference and Refined grids. The Refined grid consists of a grid size reduction by a factor 2 in the wake, around the spoiler and the exit of the underbody. The idea is to well capture the shear layers developed by flow separation at the ends of the roof and the underbody, and to capture the flow recirculation behind the vehicle. Based on the 20 prism layers, the Reference grid is made of 115M cells while the Refined grid contains 180M cells. The third grid using 30 prism layers is based on the Reference grid 3D refinement for tetrahedrons and contains 140M cells.

5 Results summary on the 25° Ahmed body

This paper is the follow-up of previous work made by the authors on Ahmed bodies [12]. The aim of this study was to fine-tune a robust numerical procedure to accurately reproduce the flow features around the four Ahmed bodies shown on Fig. 11. The reference one is named sharp edges [2]. Then, three rounded edges geometries, defined by side rounded edges, roof rounded edges and side + roof rounded edges, are studied. The rounded edges are depicted in blue on the figure.

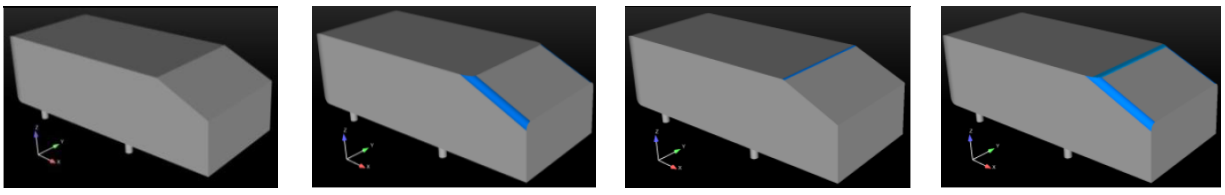

(a) Sharp edges (b) Side rounded edges (c) Roof rounded edges. (d) Side + roof rounded edges

Fig. 11: Illustrations of the four different 25° Ahmed bodies.

Here are the main conclusions concerning the turbulence modeling approach, independently of the grid used. The comparison between RANS and hybrid RANS/LES was done on the sharp edges Ahmed body. RKE leads to a non separation on the rear slant surface where as SST leads to massive separation, while separation/reattachment is expected from experiments. This separation/reattachment complex flow feature is predicted by both SAS [30], SST DDES and SST SBES [4]. However, SAS overestimates the recirculation length and SBES underestimates it. DDES is much closer to experiments. Based on these results, SST DDES model was selected as the best one for the numerical methodology to predict external aerodynamics flow.

Grid parameters were carefully analyzed during this work. For 2D mesh, Menter's criterion, detailed in Sect. 4.1.2, must be ensure to avoid GIS [26]. This leads to a minimal size of 3 mm on surfaces on the Ahmed body. Based on SST DDES model, a wall grid refinement of $y^+ < 1$ is required to resolve the viscous sub-layer. Moreover, at least 15 or 20 prism layers are necessary to accurately predict the boundary layers evolution, even if the grid with 30 layers show its superiority over flow prediction on the sharp edges case. With rounded edges, 20 prism layers were enough. In the wake of the Ahmed body, a reference length of 5 mm for the edge of the tetrahedron cells is needed to predict the flow separation on the rear part of the body.

Two time step were studied, with $\Delta_t = 1.5 \times 10^{-5}$s and $\Delta_t = 5 \times 10^{-5}$s. This was shown that both time step were able to accurately predict the flow separation on the rear window and the wake of the body, giving globally the same results. For saving of computational time, $\Delta_t = 5 \times 10^{-5}$s was selected as reference time step. A such small time step is required due to the high complexity of the flow prediction on the rear of the Ahmed body. This time step leads to a maximum CFL number of 3 in the separation area, mainly below 1 everywhere in the computational domain. A higher time step will lead to numerical dissipation and diffusion and result in a wrong prediction on the rear slant surface (no separation or massive separation for a CFL higher than 10).

This setup gives a very well prediction on aerodynamic coefficients with the $20l$ prism layers grid, on the four Ahmed bodies studied. The results are summarized on Tab. 2 and compared to experiments. The maximal error on drag prediction is 3.3% and 7.1% on lift coefficient.

In addition, a very good prediction on C_p all around the back of the bodies is shown on Fig. 12. The left part of the picture corresponds to the C_p field predicted by SST DDES while the right part is the experimental C_p field. This accurate prediction on the back leads to an accurate prediction on the drag and lift coefficients, as the main contribution for drag and lift is coming from separation on the back and wake structures.

The use of 4 different Ahmed bodies have allowed the authors to challenge and validate the numerical methodology. Indeed, the studies of sharp and rounded edges are consistent as they are present on a real vehicle. Sharp edges are found on front wheel spoiler, rear spoiler, rear window deflector and others parts of the car while rounded edges are observed around the front and the rear parts of the car. Both sharp and rounded edges are responsible of flow separation in many areas around the vehicle. Moreover, Ahmed bodies reproduce high energetic vortices on the rear part of the geometry, which are similar to the ones developed along A-pillar and C-pillar on a real car. All these geometric and flow features are similar between simplified and realistic geometries. For these reasons, the methodology described above is the starting point for the transposition on the real vehicle, in the next section. A similar approach was used by Simmonds et al. [41] to compute the cooling air drag of a car. The authors compared the simplified underhood area of the DrivAer model and two realistic cars from Jaguar Lange Rover, a large saloon and a SUV. Global numerical consistencies compared to experimental results were found between the simplified underhood area of the DrivAer model and the two realistic models.

Models	C_d Exp.	C_d	ΔC_d [%]	C_l Exp.	C_l	ΔC_l [%]
Sharp edges	0.356	0.365	2.5	0.311	0.333	7.1
Side rounded edges	0.359	0.347	-3.3	0.241	0.257	6.6
Roof rounded edge	0.298	0.299	0.7	0.333	0.337	1.2
Side + roof rounded edges	0.297	0.296	-0.7	0.254	0.255	0.4

Table 2: Comparisons of drag and lift coefficients for the $20l$ grid, $\Delta_t = 5.10^{-5}$s with DDES SST model.

6 Numerical convergence for realistic Estate vehicle

This section focuses on the comparison of the aerodynamics coefficients between the two grids detailed in Sect. 4.4: the Reference grid with 115M cells and the Refined grid with 180M cells based on 20 prism layers in the near-wall

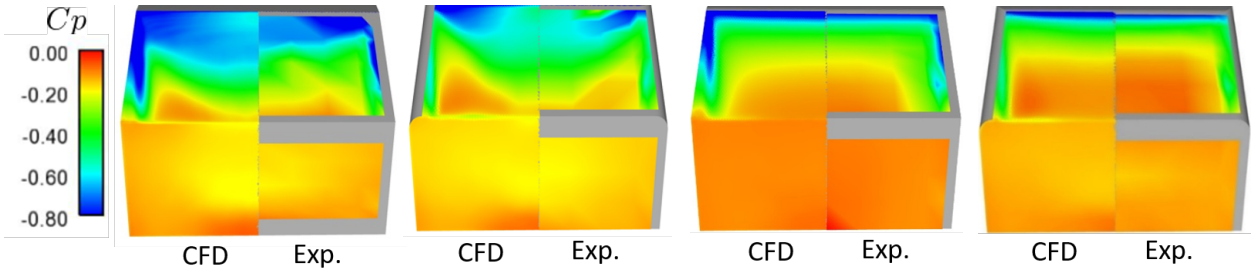

(a) Sharp edges (b) Side rounded edges (c) Roof rounded edges (d) Side + roof rounded edges

Fig. 12: C_p comparison of SST DDES results (left part) and experiments (right part) on the different 25° Ahmed bodies.

region. A third grid with 30 prism layers, using the same 3D refinement for tetrahedrons of the Reference grid, is also presented. The results are shown on Tab. 3.

First, let us focus on the grid refinement in the near-wall region, based on grids made of 20 and 30 prism layers cells. The tetrahedrons cells are identical and based on the Reference grid refinement. The drag coefficient is globally the same for the three turbulence models. This result confirms that the boundary layer discretization with 20 prism layers is enough to predict flow separation around the vehicle. Then, the tetrahedrons refinement is studied based on the Reference and the Refined grids. The comparisons of drag C_d results on the two grids show that the results are consistent for the three turbulence modeling approaches, RKE EWT, SST and SST DDES. Drag coefficient is very well predicted for both RANS models while a slightly larger difference is obtained with DDES. Lift prediction is globally not accurate for all cases. It is well known that it is more difficult to predict lift than drag. Moreover, a non negligible part of the lift discrepancy comes from the experiments. Indeed, due to the fact that there were no wheels touching the ground, the aerodynamics balance of the wind tunnel, detailed in Sect. 3, may have been affected. For this reason, the lift comparison with experiments is not shown in this paper.

At this stage, it is clear that hybrid RANS/LES methods do not show better prediction than RANS models on aerodynamics loads on a realistic car geometry. This behavior is well known for DDES or LES ([11], [47]) or PANS [32], [53]. In fact, the good prediction on C_d for RANS models are linked to errors cancellation all around the vehicle. Fig. 13 shows the cumulative drag SC_d along the vehicle for RKE and DDES models. The main differences between the two models globally appear when separations occur: around the front fairings, the rear fairings and the back. Around the front fairings, for $X \in [-0.5; 0.4]$ m, DDES underestimates drag compared to RKE. Then, until the rear fairing, for $X \in [0.5; 2.5]$ m, the value is almost the same between RANS and DDES. It means that the main difference between the two models takes place on the rear part of the vehicle, for $X > 2.5$ m. We will see in the next section that both the surface pressure distribution (directly linked to drag value) and the global 3D flow prediction are highly enhanced using hybrid RANS/LES method compared to RANS models, especially $X > 2.5$ m. For this reason, there is no valid reason that RANS predicts a more accurate C_d than DDES.

Fig. 14 compares the streamwise Vx and vertical Vz velocities in the symmetry plane $Y0$ for the DDES model on the two grids. The results are almost exactly the same for Vx and Vz velocities. The same comparisons with RANS models, not shown here for space reasons, show the same trend. Moreover, the flow comparison with experiments show very good agreement for DDES model. The comparison between RANS and DDES is done on Fig. 17 in the next section. RANS prediction is not accurate compared to DDES. To conclude, the grid refinement in the wake and around the underbody of the car does not show any significant improvement in the flow prediction. Consequently, the Reference grid is used for the reminder of this work, in order to save computational resources.

		20 prism layers		30 prism layers	
Grids	Models	C_d	ΔC_d	C_d	ΔC_d
-	Exp.	0.244	-		
Reference	RKE EWT	0.242	-0.002	0.242	-0.002
Reference	SST	0.242	-0.002	0.241	-0.003
Reference	DDES SST	0.255	0.011	0.254	-0.010
Refined	RKE EWT	0.243	-0.001		
Refined	SST	0.249	0.005		
Refined	DDES SST	0.254	0.010		

Table 3: Comparisons of drag coefficient for RKE, SST and DDES SST (realistic Estate vehicle).

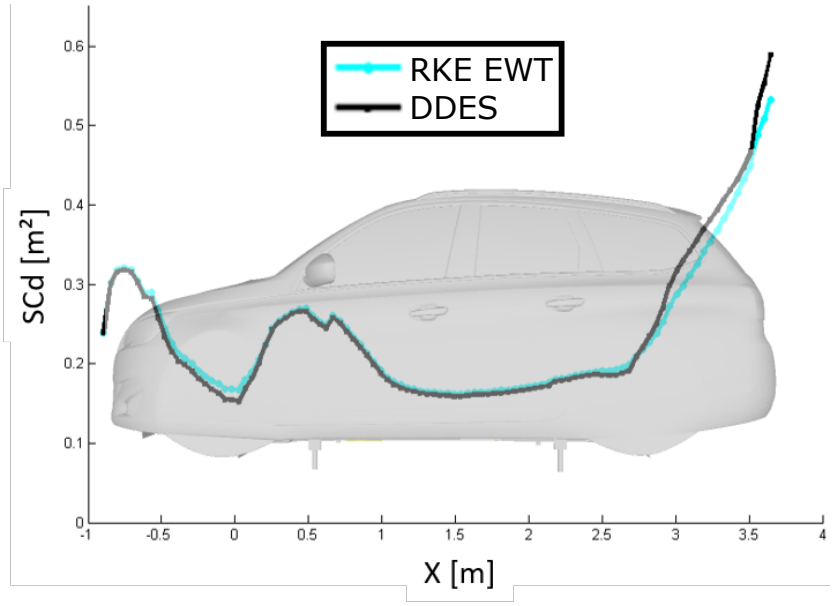

Fig. 13: Plot of the cumulative drag along the longitudinal axis of the vehicle.

7 Surface and volume comparisons of turbulence modeling approaches

Following the preliminary study published by the authors [13], a detailed analysis of the flow features around the vehicle is made hereafter. This section compares 2D and 3D results with RKE and SST RANS models, as welle as SST DDES hybrid RANS/LES method. Results are compared along the roof, the back, the right side, the underbody and the wake of the vehicle using pressure coefficient taps, PIV and tomographies.

7.1 Roof

Pressure coefficient along the roof of the vehicle is depicted on Fig. 15. Experiments is presented in red color, while SST DDES is in blue, SST in yellow and RKE in gray. The left part of the picture is dedicated to the 7 probes along the Y0 line of the car and the right part to the 5 probes along Y250 line. On Y0 line, RANS models provide the better accuracy compare to experiments. From probe 4, a small offset is visible with DDES and keep until the end of the roof at probe 7. On Y250 line, there is more discrepancy for three turbulence models all along the 5 probes. DDES gives a better prediction at probe 5, close to the separation area between the roof and the rear window.

7.2 Back of the car

This part focuses on the flow separation at the end of the roof and the wake behind the vehicle. Fig. 16 compares the pressure coefficient on the back of the car, along the Y0 and Y500 lines. On the graphics, the probes are divided into three areas: the roof, the rear window and the rear bumper. First, let us focus on the symmetry Y0 line. As previously seen on Fig. 15, RANS prediction is better on the roof, from probes 1 to 3. Then, at probe 4, massive separation occurs as the flow is detached from the end of the roof. Then, SST DDES perfectly match experiments in the wake, from probes 4 to 9. The same behavior is observed along the Y500 line. In the separation area, from probes 21 to 26, DDES prediction matches very well the experiments. From these graphics, we can conclude that the separation from the roof is well predicted, as well as the separation from the underbody (as the C_p prediction is very accurate on the bumper), only for DDES model. These results clearly indicate the superiority of DDES approach, due to the use of LES formulation in separated area allowing the resolution of smaller turbulent scales compared to RANS solutions.

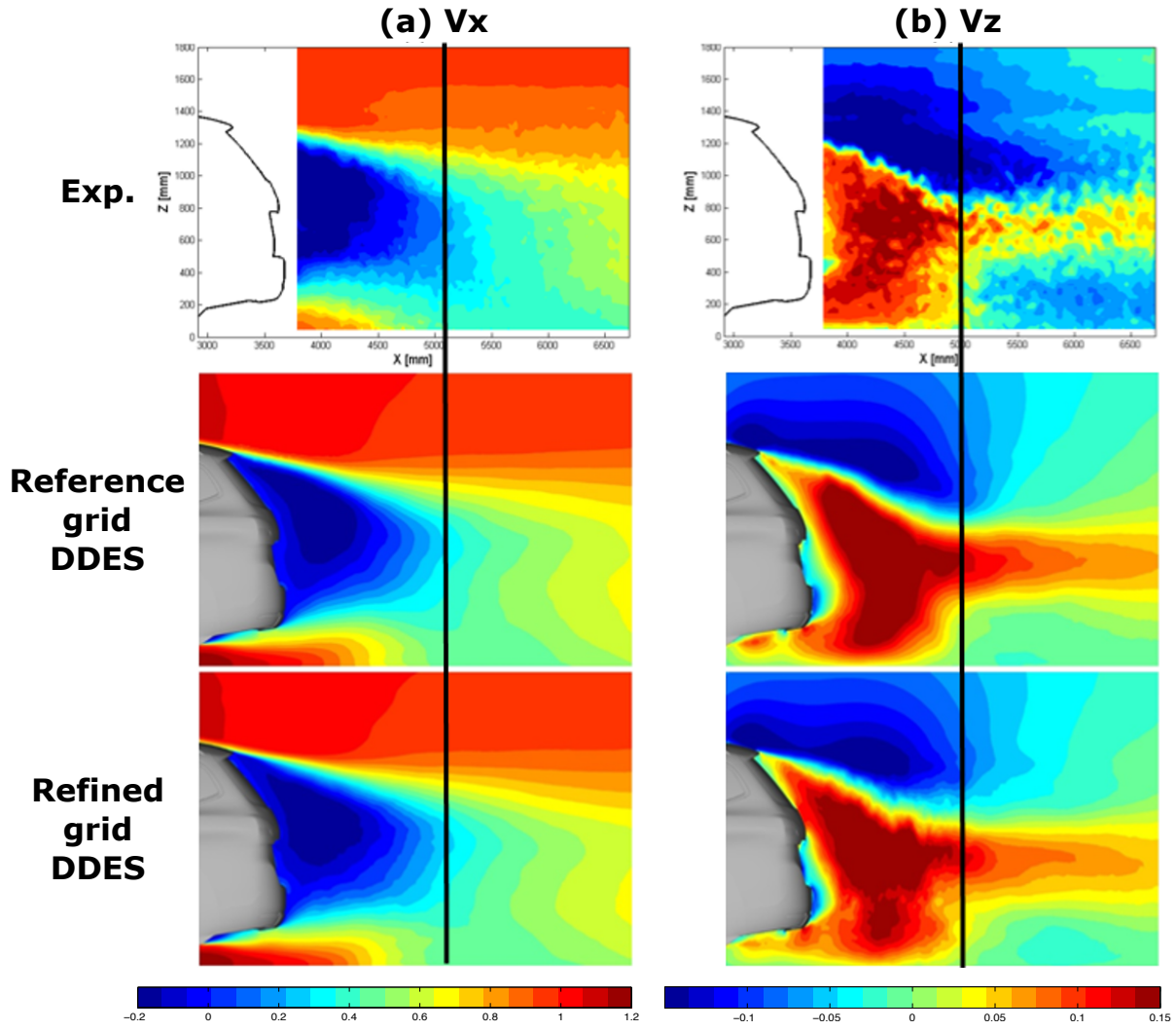

Fig. 14: Comparisons of streamwise and vertical velocities on symmetry plane $Y0$ for REF and RAF grids.

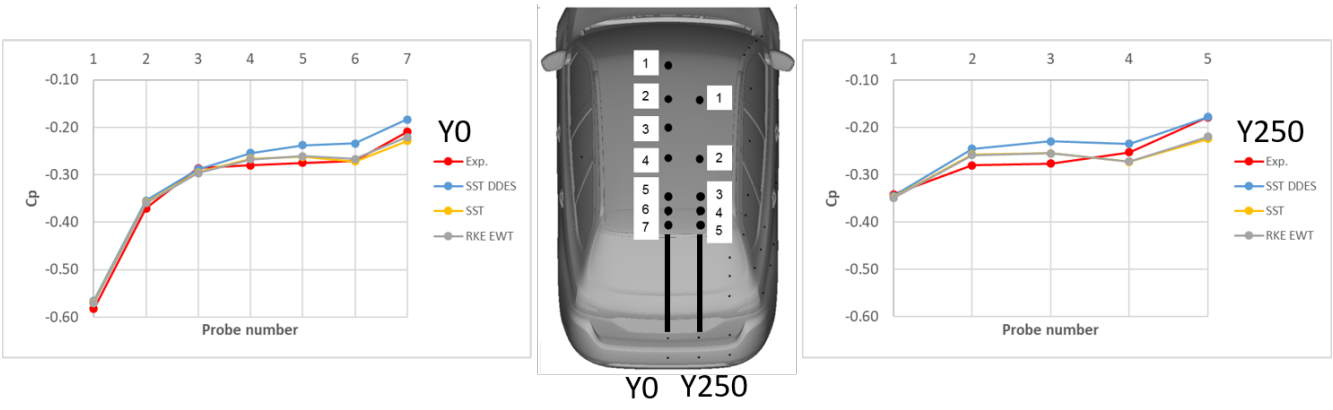

Fig. 15: Comparisons of pressure coefficients evolution on the roof of the vehicle on Y0 and Y250 lines.

The streamwise V_x and vertical V_z velocity is presented on Fig. 17. RKE, SST and SST DDES results are compared to experimental tomography in the symmetry plane Y0. At one glance, it is obvious that DDES shows very good agreement on both V_x and V_z velocities compared to experiments. On the V_x plot, the size of the recirculation bubble, in blue, is far better predicted by DDES. Regarding the flow coming from the underbody, once again, DDES shows the best prediction. RANS present high speed velocity coming out of the underbody, far in the wake, which is not present

in experiments. For the V_z velocity, only DDES predicts the accurate shape and intensity level of V_z contours. These two results mean that DDES is able to reproduce very well the V_x and V_z shape of the wake. This is confirmed by Fig. 18 that represent the streamlines and the spanwise vorticity Ω_y. The streamlines predicted by DDES perfectly match the experiments. From a physical point of view, the flow coming from the underbody moves upwards into the wake and is bounded on the top by the flow coming from the roof. With SST, two massive separation bubble are predicted, showing that the flow coming from the roof is dominant on the flow coming from the underbody, which is not accurate compared to experiments. RKE is better than SST, but less predictive compared to DDES. The vorticity plot definitively shows the DDES superiority over RANS models. The shape of the shear layers and their intensity are almost perfectly predicted, explaining why the global wake of DDES in the Y0 plane is so close to experiments. Fig. 19 compares RKE, SST and SST DDES results to experiments in Z970 plane. This plane corresponds to the middle plane in the upper part of the wake, depicted in cyan on Fig. 5. In this area, RKE shows a better prediction regarding the streamwise velocity V_x compared to SST models. The separation length is slightly underestimate with both SST RANS and SST DDES models. The streamlines comparisons show a global accurate prediction for both RKE and SST DDES.

7.3 Sides

The flow on the right part of the vehicle is now studied on Fig. 20. Three lines of pressure coefficients are represented. L1 corresponds to the upper part of the vehicle. L1 is made of 5 probes from probe 37 on the front side window to probe 41, close to separation area at the junction between the side and the rear window. L2 is under L1, corresponding to the middle part of the rear window on the side of the car. L2 is made of 3 probes from 42 to 44, with 44 is close to separation area. Finally, L3 is at the bottom part of the rear window. L3 is made of 5 probes from probe 45 on the front door to probe 49 on the rear right lump.

First, let us have a look on the C_p prediction along the vehicle sides. It corresponds to L1 with probes 37 to 40, L2 with probes 42 and 43 and L3 with probes 45 to 48. Globally, all models predict well the C_p in this area, even if an offset on absolute value is observable. The differences observed between the three turbulence models can be attributed to the turbulent nature of the flow. This turbulence is likely caused by the presence of the door handle and the junction between the door and glasses. The main interesting part on these plots are located close to separation areas, represented by probe 41 for L1, probe 44 for L2 and probe 49 for L3. From L1 and L2, the same trend is observable for the turbulence models. SST is very close to experiments, meaning that the location of the separation point is accurately predicted. RKE over-predicts C_p while DDES under-predicts it. The surfaces are rounded in these two locations. This result confirms once again that it is more difficult to predict separation point on curved surface. However, on probe 49 on L3, the rear lump is sharp, leading to a separation point control directly by the geometry. In this configuration, DDES is more accurate and close to experiments. These results are consistent with the findings made by the authors on

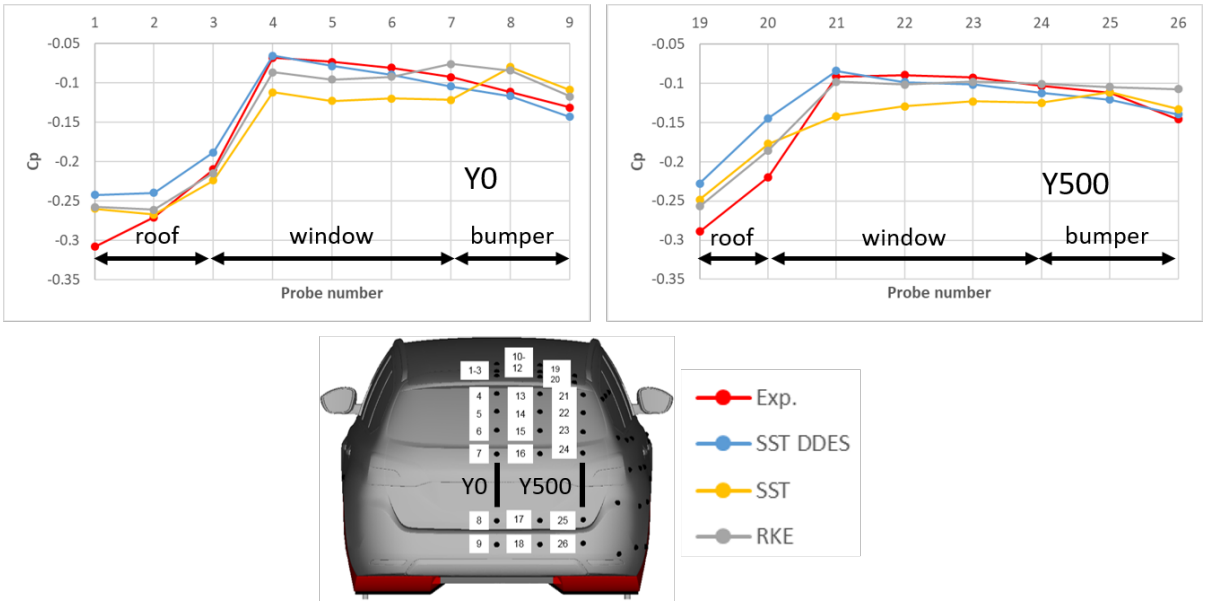

Fig. 16: Comparisons of pressure coefficients evolution on the rear of the vehicle on Y0 and Y500 lines.

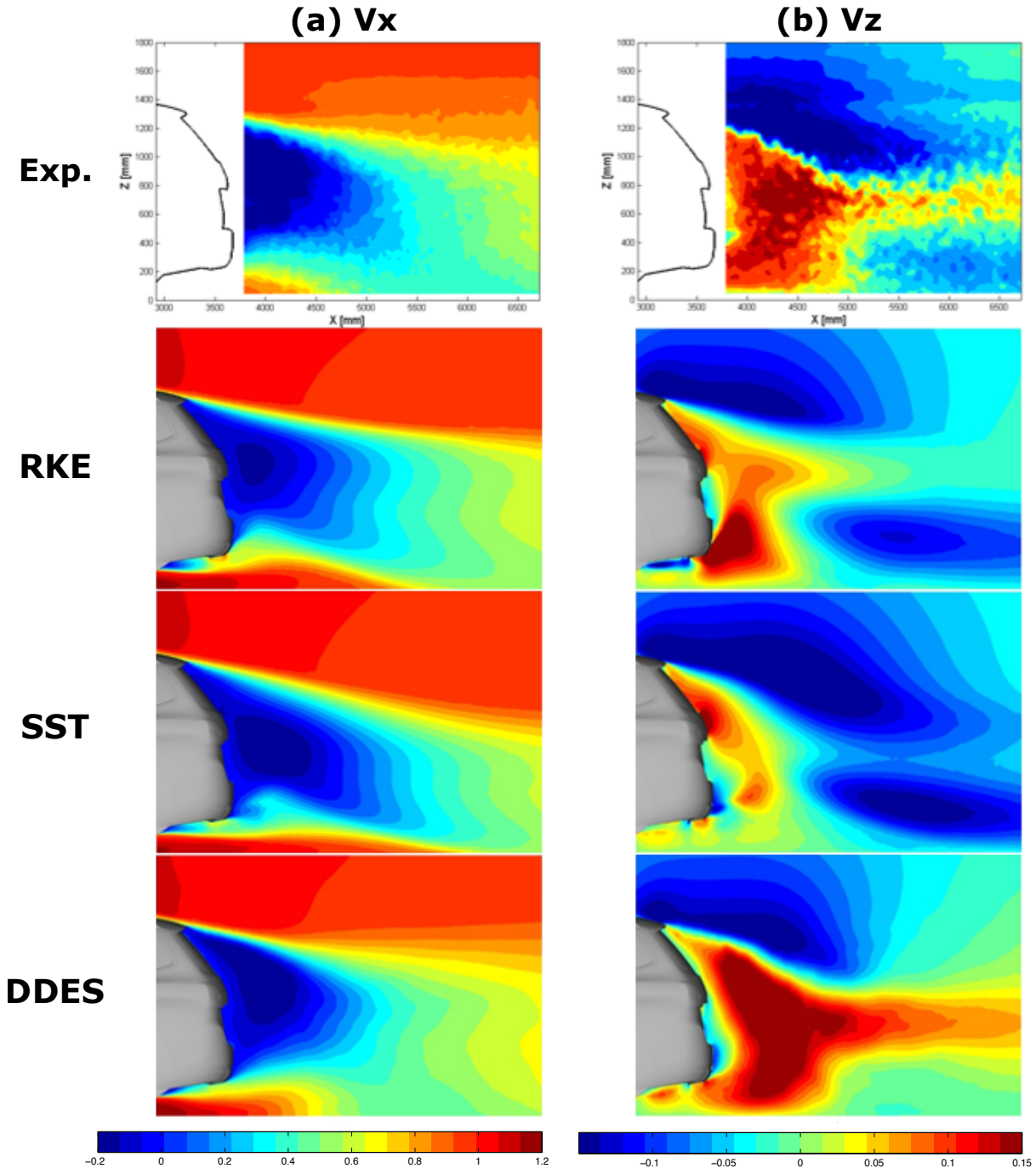

Fig. 17: Comparisons of streamwise V_x and vertical V_z velocities on Y0 plane between RKE, SST and SST DDES vs experiments.

the study of the sharp and rounded edges 25° Ahmed bodies [12]. To improve DDES prediction on rounded separation area, the first attempt would be to try to refine the mesh. However, this may lead to LES intrusion inside the boundary layer and finally GIS. This is why the user has to be really careful on the grid size. A specific grid size comparison has been done along L1 line. The default value is 3mm. Then, two other surface grids has been made with 6mm and 10mm. Fig. 21 shows that using larger size mesh, 6mm or 10mm, provide better results in rounded separation area. In fact, the 3mm grid is too fine and leads to GIS. The 6 mm grid is then advised in such area of the vehicle.

As we have seen previously, C_p are well predicted on the Y500 line on Fig. 16, mainly because the streamwise velocity V_x is well predicted, as presented on Fig. 22. Indeed, the streamwise velocity is preponderant in the computation of the norm of velocity vector. Nevertheless, vertical velocity V_z is not so well predicted for the three turbulence models. It is clear from experiments that the flow around the rear windows is going down to the ground. In computations,

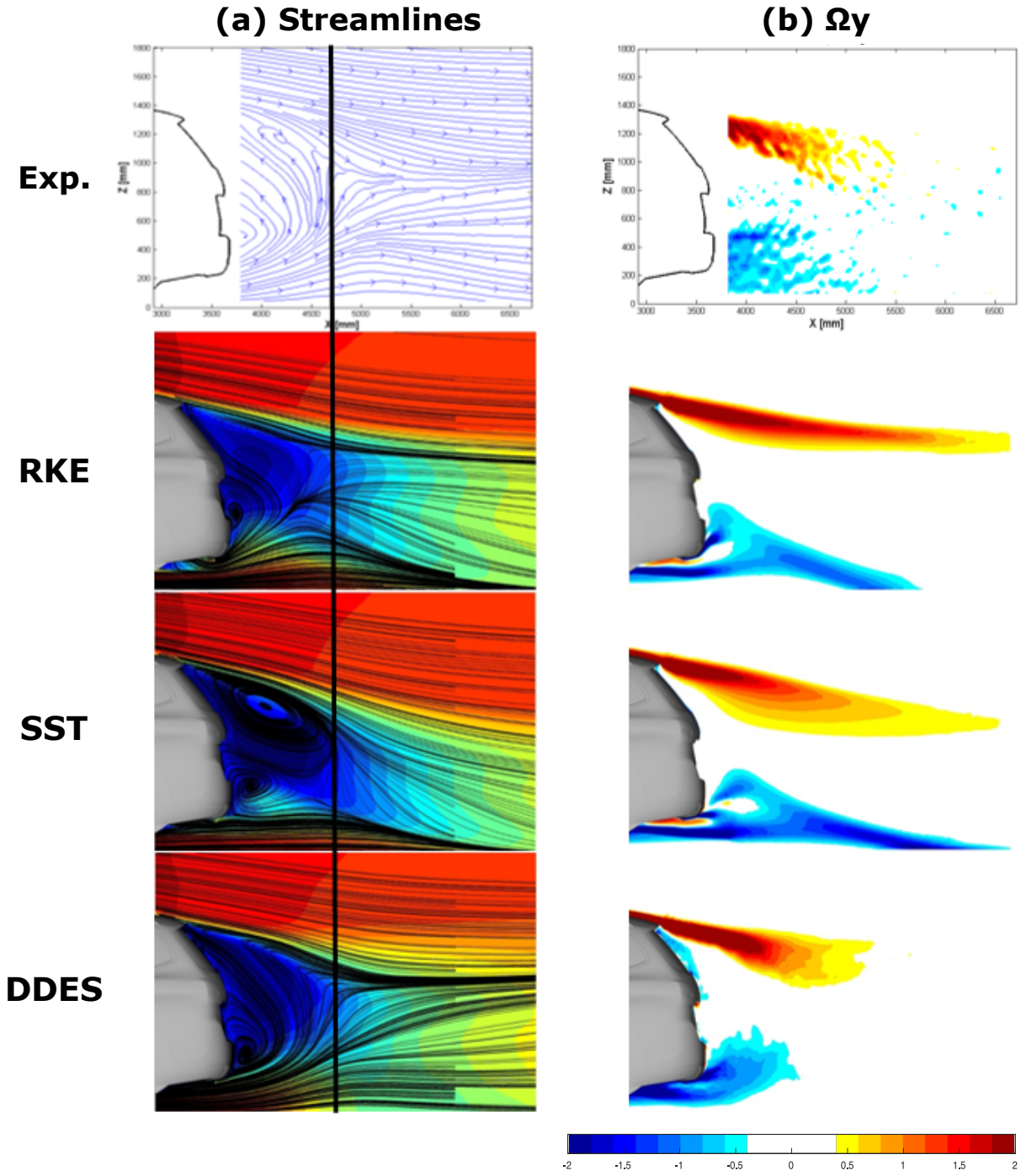

Fig. 18: Comparisons of streamlines and vorticity Ω_y on Y0 plane between RKE, SST and SST DDES vs experiments.

we can observe different size of recirculation in this area. These results confirmed the complexity to predict separation area and flow features around rounded surfaces.

7.4 Fairings

The flow in the wake of the right rear fairing is numerically studied and compare to experimental 2D PIV on Fig. 23. Streamlines are depicted in the area as it provides easiest way to observe the size and shape of the separation area. RANS and DDES have opposite trend in this flow location. SST predicts a massive separation. RKE computes a larger recirculation area versus experiments, but closer to experiments in comparison with SST. On the contrary, DDES predicts a smaller recirculation bubble in the wake of the fairing. These results show the difficulty to predict the flow

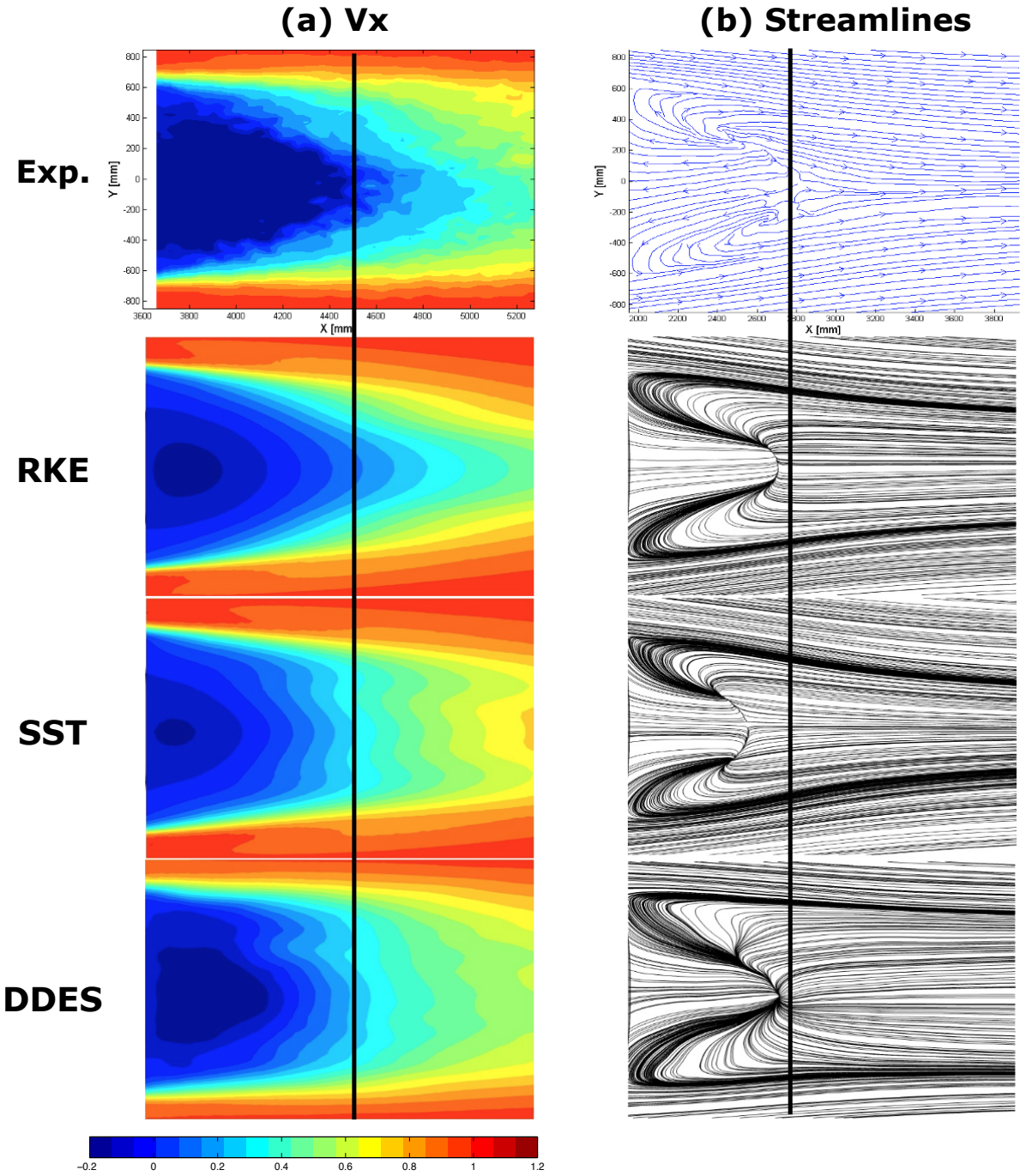

Fig. 19: Comparisons of streamwise velocity and streamlines on Z970 plane between RKE, SST and SST DDES vs experiments.

around the fairings. Separation generated by the spoiler on the fairings, as well as ground effect, lead to very complex flow region. Some tests on surface and volume grid refinement have been carried out, without any significant change in separation prediction. Even though the computation around the fairings is not perfect, we have seen previously on Fig. 17, Fig. 18, Fig. 22, and on next section on Fig. 25 and Fig. 26, that the global flow coming at the exit of the underbody is very accurately predicted using DDES.

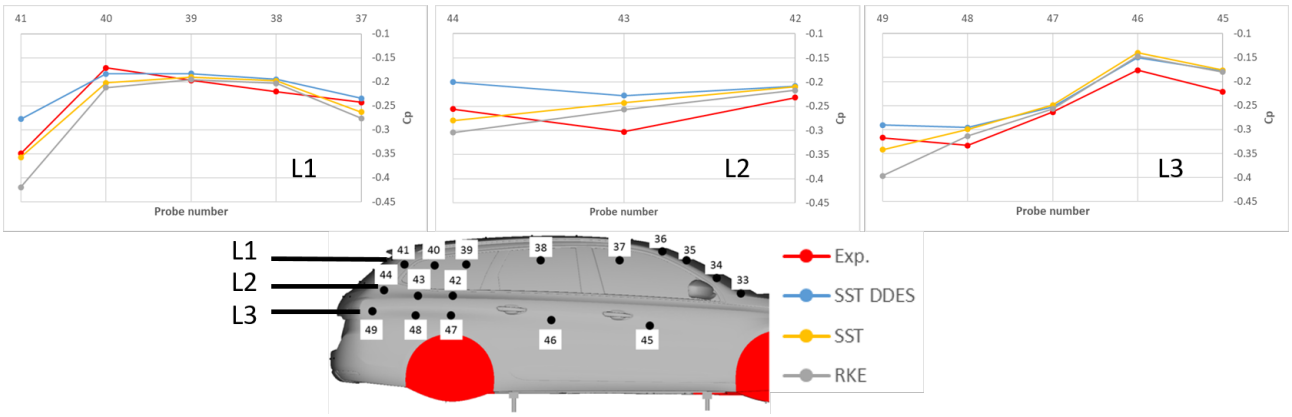

Fig. 20: Comparisons of pressure coefficients evolution on the side of the vehicle along lines L1, L2 and L3.

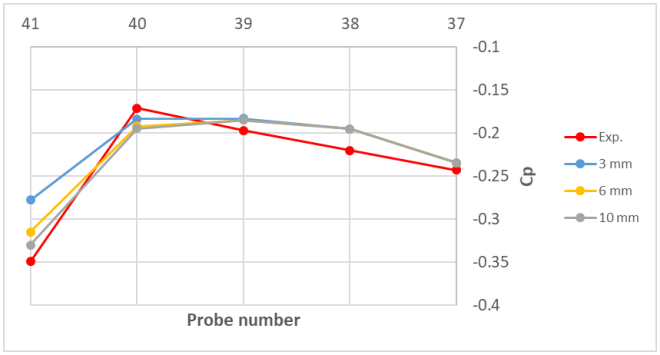

Fig. 21: Comparisons of pressure coefficients evolution on the side of the vehicle along lines L1, L2 and L3.

7.5 Underbody

Pressure coefficients on the underbody are presented on Fig. 24. Two lines on Y0 and Y350 planes are computed and compared to experiments. On Y0 line plot, DDES globally captures well the C_p evolution. On Y350 line, prediction is quite good except around probes 15 to 17, without any explanation. Close to separation area, for probes 9 and 10 on Y0 line and probes 19 and 20 on Y350 line, DDES shows the best agreement. In fact, at the rear of the underbody, a small step can be observable on the figure between probes 9 and 10 and 19 and 20. Besides, at the end of the underbody, the flow separates again. Around separations, DDES shows once again its superiority on the prediction flow. Probe 19 is missing from experiments.

Fig. 25 and Fig. 26 respectively present V_x and V_y velocities and V_z and streamlines comparisons in the plane Z320 between experiments and computations. On these four graphs, DDES shows an almost perfect match regarding experiments. Intensity of velocities, shape of recirculation, flow going in x, y and z directions are very accurately predicted. At this location, RKE and SST overestimates the recirculation behind the car. These results show that DDES accurately compute the flow coming from the underbody. As the wake topology is mainly guided by the underbody, it explains why DDES shows very nice prediction on Fig. 17 and Fig. 18.

7.6 Wake

In this section, the flow in the wake of the vehicle is studied in the cross-section plane X100, which is located 100 mm behind the rear bumper. Fig. 27 and Fig. 28 respectively present V_x and V_y velocities and V_z and streamwise vorticity Ω_x comparisons in the plane X100 between experiments and computations. Regarding V_x, the width of the wake is the same for all turbulence models for $400 < Z < 1200$ mm. Main differences appear in the underbody area, for $-700 < X < -500$ mm and $0 < Z < 200$ mm. RANS models show a massive expansion of the flow towards outside compared to experiments and DDES. The global flow is very accurate with DDES. V_z results show the very good prediction of DDES both behind the rear windows and the rear bumper. This means that the global wake is well captured

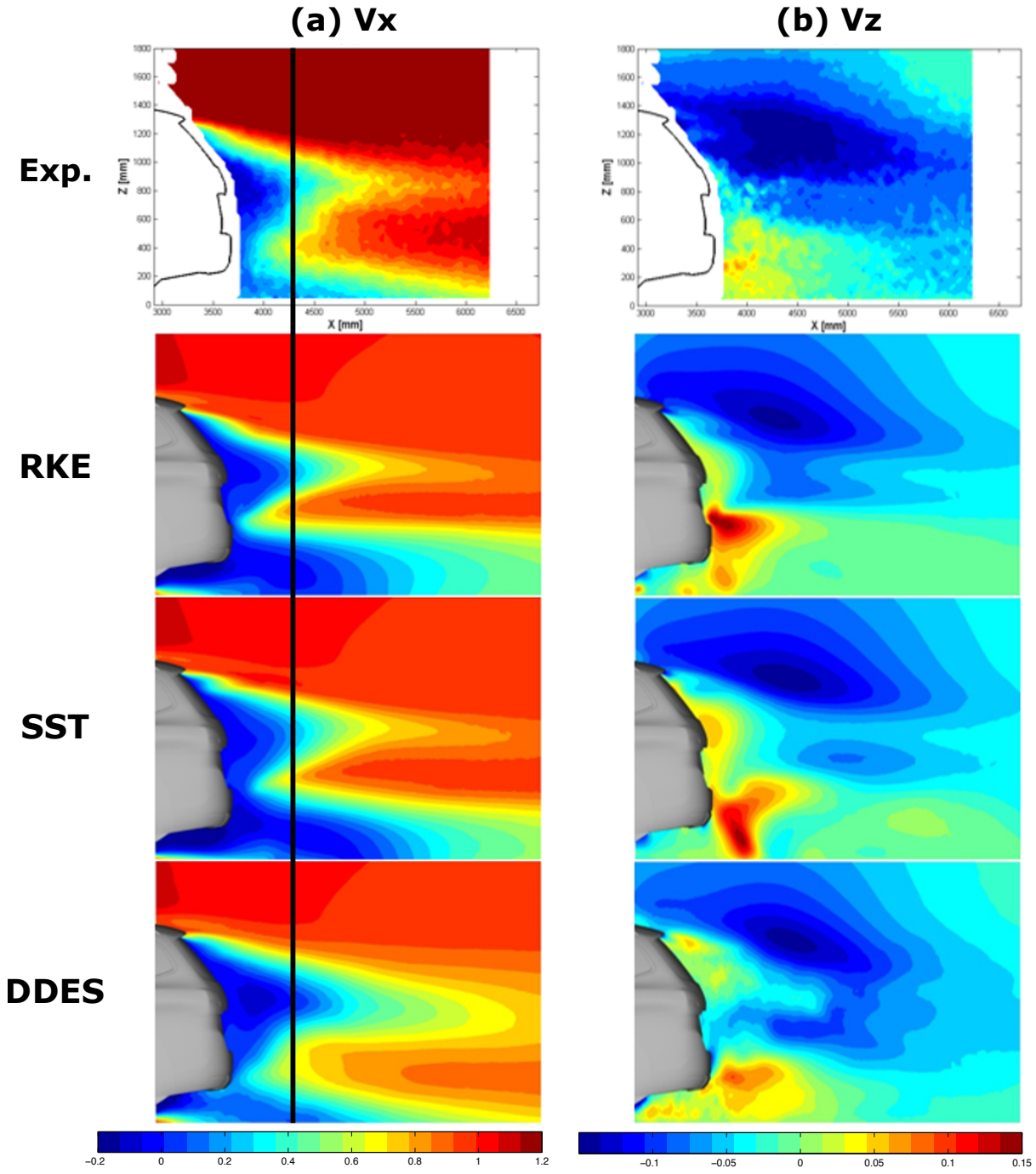

Fig. 22: Comparisons of streamwise V_x and vertical V_z velocities on Y500 plane between RKE, SST and SST DDES vs experiments.

compared to RANS that globally fail. V_y and Ω_x allow us the visualize the position of the turbulent structures generated around the vehicle. Regarding the vorticity, it is clear that 4 structures arise: 1. comes from the A-pillar vortex, 2. is build up by the roof rack on the car, 3. is created by the side mirrors and 4. is generated by the separation around the rear lump and bumper. With RANS, due to averaging on Navier-Stokes equations, only large structures remain at the end of the computation. On the contrary, for DDES model, due to LES switch, the model is able to resolve smaller turbulent scales. Moreover, intensity of turbulent structures is overestimated with RANS models. By transparency, it is important to notice that the measured flow from experiments is a bit noisy, due to tomography procedure measurements.

To conclude on this three-dimensional flow features analysis, it is clear that the flow around a realistic vehicle, at scale 1:1, is very complex. There are many areas of separations, around A-pillar vortices, side mirrors, end of the roof, fairings, end of the underbody, sides of the back, etc. Moreover, the most complex part is the wake, where the flow

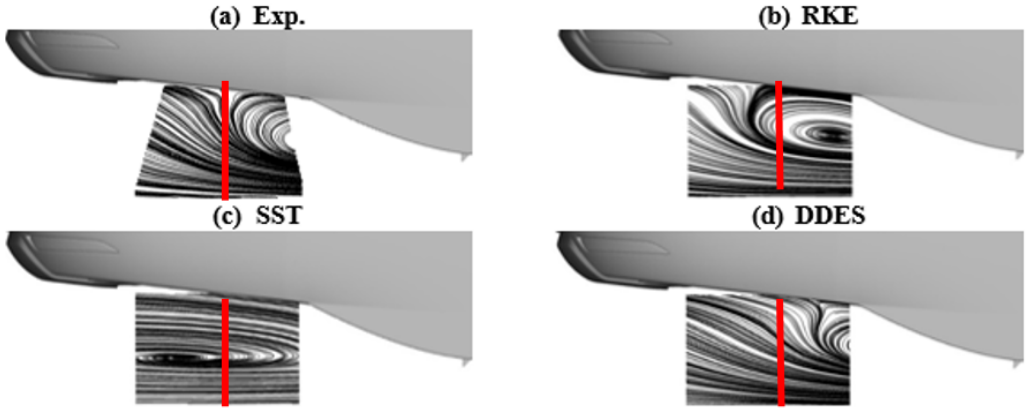

Fig. 23: Comparisons of streamlines in the wake of the rear right fairing between experiments and computations.

coming from the underbody moves upwards into the wake and is bounded on the top by the shear layer coming from the roof separation. This flow feature occurs on one hand, due to massive separation on the roof, and on the other hand, because the underbody exit has an ascending slope creating a diffuser behavior and pushing the flow upwards. This mechanism generates one large recirculation bubble in the back of the car (see Fig. 18) and is very typical of an Estate shape compared to more classical wake with 2 recirculation bubbles, one on each other, for Notchback or Fastback geometries. As a consequence, this area of the flow is responsible of more than one third of the total drag contribution. As described before, predicting the whole flow features is not an easy task using CFD. However, looking at the global picture, it is obvious that DDES, using specific grid refinement in area of interest, is able to globally reproduce very well the flow features around the vehicle. The user has to find the right balance between accuracy with DDES and low computational cost with RANS. A RANS computation on 384 cores lasts around 2 hours. A DDES computation on 1152 cores is around one day and a half long. The hybrid RANS/LES simulation is 18 times more expensive than the RANS computation.

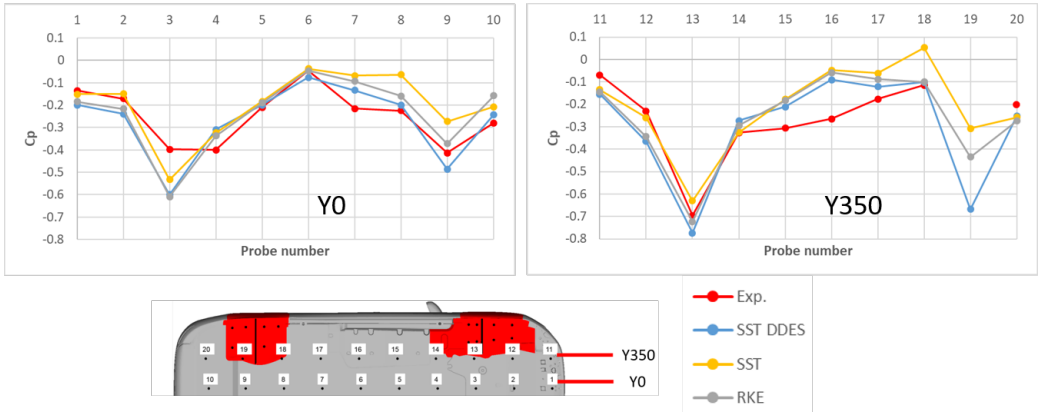

Fig. 24: Comparisons of pressure coefficients evolution on the underbody along Y0 and Y350 lines.

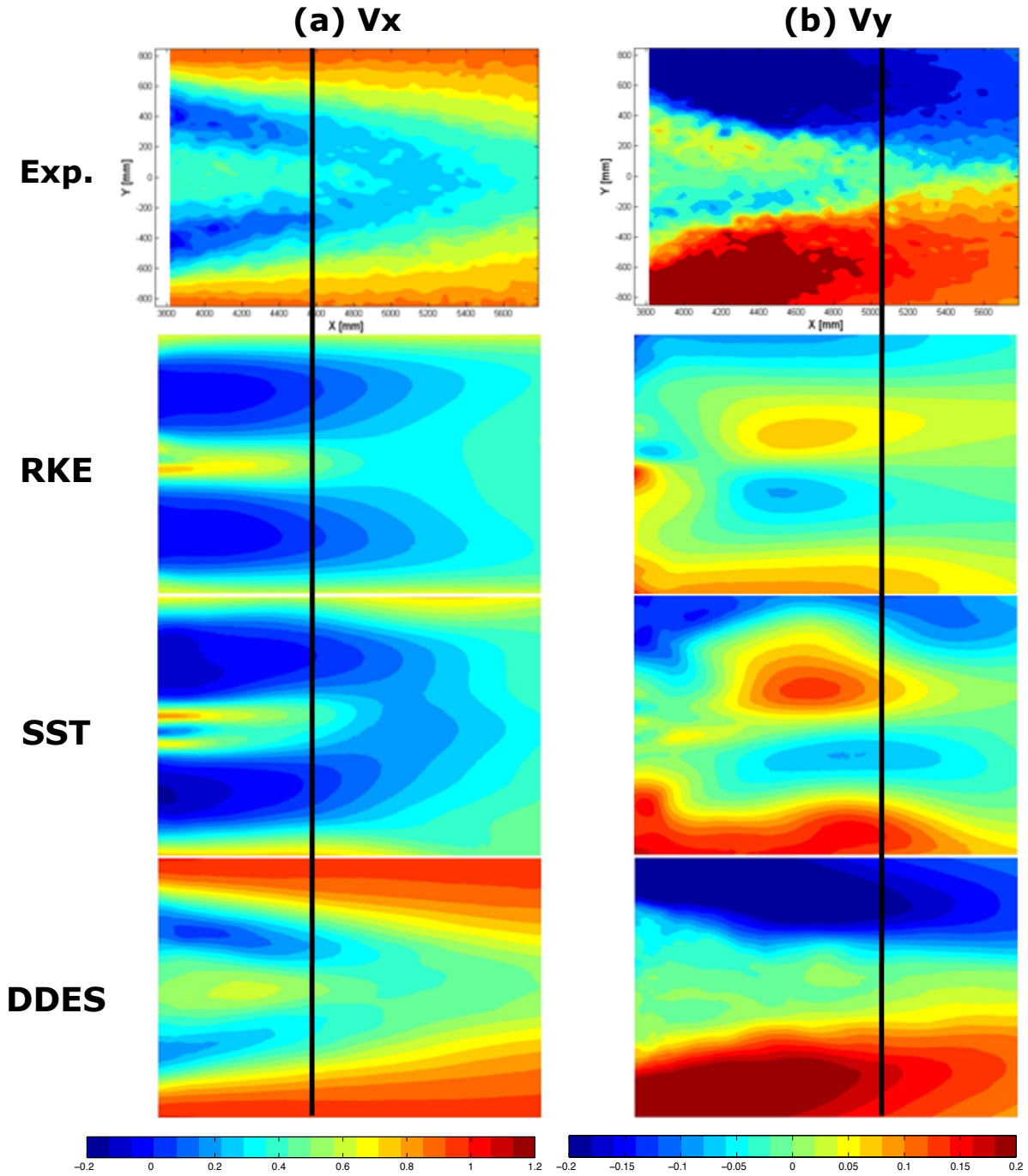

Fig. 25: Comparisons of streamwise V_x and spanwise V_y velocities on Z320 plane between RKE, SST and SST DDES vs experiments.

8 Conclusions

To achieve accurate simulations of the flow around real car geometries, robust and accurate numerical procedures are required. Usually, RANS is performed in the industry for its robustness and low computational cost, even if RANS are enable to capture flow unsteadiness. The aim of this work was to use the best Scale-Resolving Simulation procedure to compute and accurately reproduce the flow around a realistic Estate vehicle. Here, RKE and SST RANS, as well as the DDES hybrid turbulence approaches were studied and compared to in-house experiments on the Peugeot Estate car. The framework and initial/boundary conditions for computations were designed based on the wind tunnel experimental conditions. The grid refinement was adapted depending on shear strengths generated in different areas of the flow. Comparisons of 20 and 30 prism layers grids showed that the boundary layer computation was fine enough with

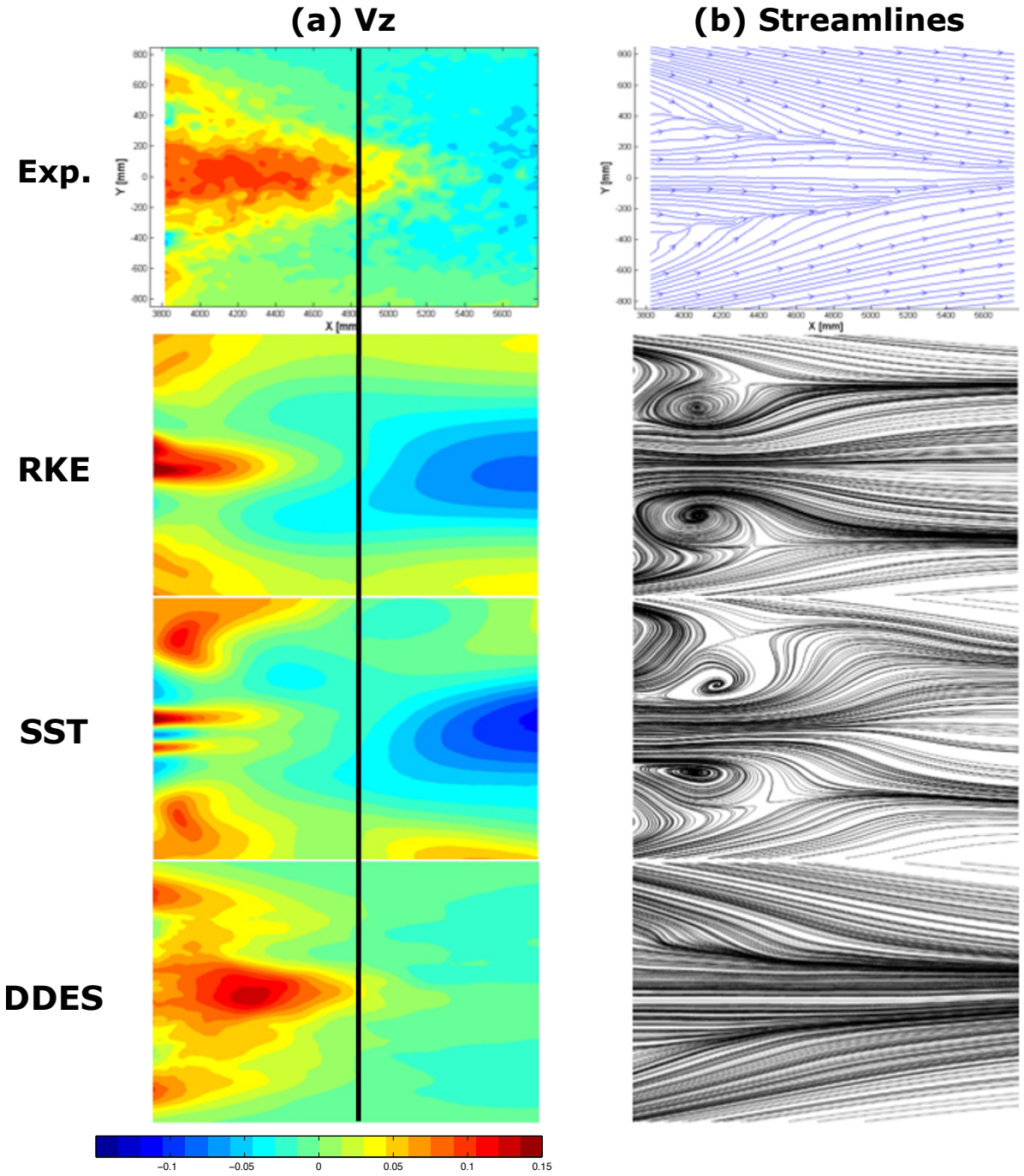

Fig. 26: Comparisons of vertical V_z velocity and streamlines on Z320 plane between RKE, SST and SST DDES vs experiments.

20 prism layers, leading to constant drag coefficient prediction. Moreover, the Reference grid with 115M cells was compared to the Refined grid with 180M cells. The drag comparison shows that RKE is more accurate than SST and DDES SST. Comparisons of the flow features on the two grids were studied and did not show any significant difference between them. Consequently, the Reference grid was chosen to reduce the numerical cost of the study. Then, a detailed topological analysis was performed in order to estimate the prediction of the near wake topology by different techniques compared to experiments. The study covered several cut planes to represent the 3D features of the flow structures. The overall best flow prediction was obtained with the SST DDES model, as RKE and SST suffer from predicting the shape and length of the recirculation bubbles in the wake of the vehicle. In fact, it was demonstrated that even if RANS models generate equivalent accurate overall drag coefficient with DDES and experiments, this accuracy is mainly due to the ”compensation” effects between different parts of the vehicle. However, the topology of the rear near wake was more accurately computed using the DDES method. The reason for this accuracy using DDES model is the better

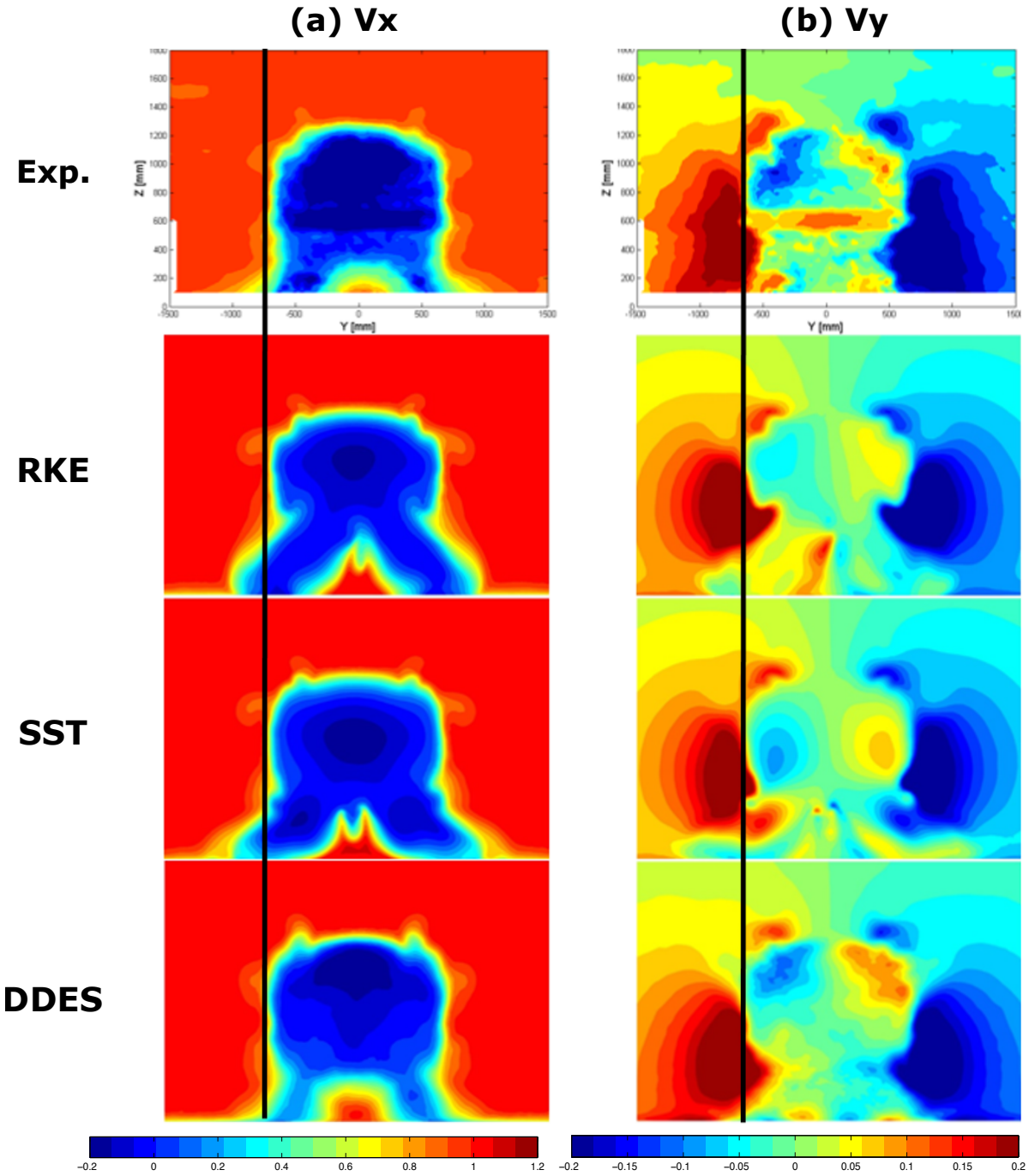

Fig. 27: Comparisons of streamwise V_x and spanwise V_y velocities on X100 plane between RKE, SST and SST DDES vs experiments.

resolution of the wake structures and shear mechanisms using the LES method in separated areas of the flow. It was shown that the flow coming from the underbody moves upwards into the wake and is bounded on the top by the shear layer coming from the roof, generating one large recirculation bubble in the back of the car. Hybrid RANS/LES models have shown superiority over RANS turbulence model for predicting the flow over the Estate vehicle with a reasonable computational cost. In this paper, the near wake topology and wall pressure values on the Peugeot Estate car model were simulated, reinforcing the previous literature results, demonstrating the performance of hybrid RANS/LES methods to predict the flow around realistic vehicles.

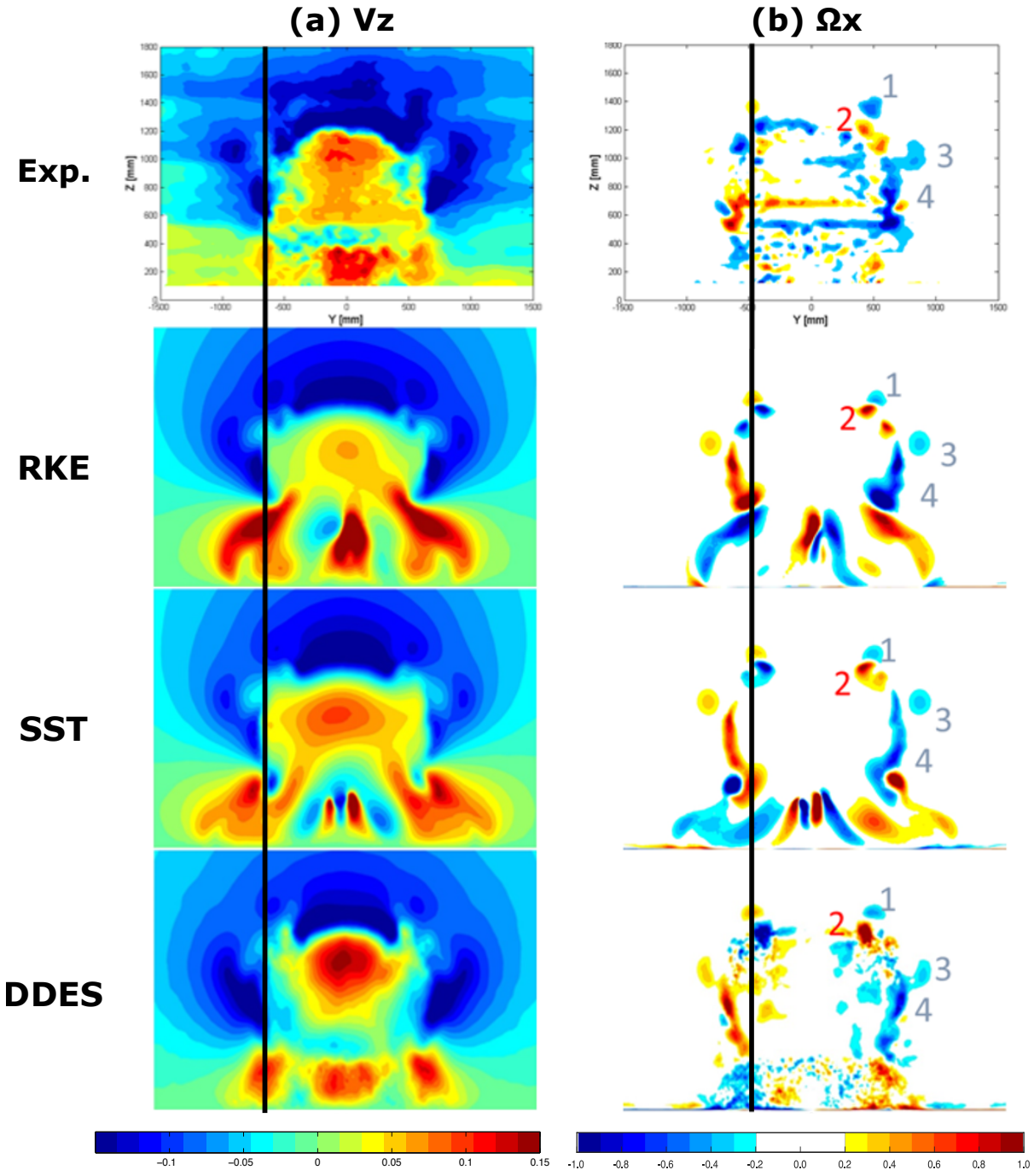

Fig. 28: Comparisons of vertical V_z velocity and streamwise vorticity Ω_x on X100 plane between RKE, SST and SST DDES vs experiments.

References

1. Adams, Nikolaus A., and Stefan Hickel. "Implicit large-eddy simulation: Theory and application." Advances in Turbulence XII: Proceedings of the 12th EUROMECH European Turbulence Conference, September 7-10, 2009, Marburg, Germany. Berlin, Heidelberg: Springer Berlin Heidelberg, 2009.
2. Ahmed, S. R., G. Ramm, G. Faltin. Some salient features of the time-averaged ground vehicle wake. *SAE Technical Paper Series* 840300, Detroit, 1984.
3. Angelis, W., Drikakis, D., Durst, F., Khier, W. Numerical and experimental study of the flow over a two-dimensional car model. Journal of wind engineering and industrial aerodynamics, 62(1), 57-79, 1996.
4. ANSYS Fluent Theory Guide, 2020R2, 2020.
5. Ashton, N., & Revell, A. Investigation into the predictive capability of advanced Reynolds-Averaged Navier-Stokes models for the DrivAer automotive model. In The International Vehicle Aerodynamics Conference, 2014.

6. Ashton, N., West, A., Lardeau, S., & Revell, A. Assessment of RANS and DES methods for realistic automotive models. Computers & Fluids, 128, 1-15, 2016.
7. Avadiar, T., Thompson, M. C., Sheridan, J., & Burton, D., Characterization of the wake of the DrivAer estate vehicle. Journal of Wind Engineering and Industrial Aerodynamics, 177, 242-259, 2018.
8. Bae, H., Lozano-Durán, A., Bose, S., Moin, P. Dynamic slip wall model for large-eddy simulation. Journal of Fluid Mechanics, 859, 400-432, 2019.
9. Cogotti, A. A parametric study on the ground effect of a simplified car model. SAE transactions, 180-204, 1998.
10. Deck, S. Zonal-detached-eddy simulation of the flow around a high-lift configuration. AIAA journal, 43(11), 2372-2384, 2005.
11. Delassaux, F., Etude de l'écoulement externe instationnaire autour d'un profil de véhicule, Stage de fin d'études Ingénieurs, Plastic Omnium, 2014.
12. Delassaux, F., Mortazavi, I., Itam, E., Herbert, V., & Ribes, C. Sensitivity analysis of hybrid methods for the flow around the ahmed body with application to passive control with rounded edges. Computers & Fluids, 214, 104757, 2021.
13. Delassaux, F, Mortazavi, I, Herbert, V, Ribes, C. Flow Simulation and Investigation Around a Estate Vehicle Using Hybrid Methods. Proceedings of the ASME 2022 Fluids Engineering Division Summer Meeting. Volume 2: Multiphase Flow (MFTC); Computational Fluid Dynamics (CFDTC); Micro and Nano Fluid Dynamics (MNFDTC). Toronto, Ontario, Canada. August 3-5, 2022. V002T05A011. ASME.
14. Drikakis, Dimitris, et al. Large eddy simulation using high-resolution and high-order methods. Philosophical Transactions of the Royal Society A: Mathematical, Physical and Engineering Sciences 367.1899 (2009): 2985-2997, 2009.
15. Fotiadis, G., Skaperdas, V., Iordanidis, A. The influence of mesh characteristics on Openfoam simulations of the DrivAer model, 6th BETA CAE International Conference, 2015.
16. Goc, K. A., Lehmkuhl, O., Park, G. I., Bose, S. T., Moin, P. Large eddy simulation of aircraft at affordable cost: a milestone in computational fluid dynamics. Flow, 1, E14, 2021.
17. Guilmineau, E. Numerical simulations of flow around a realistic generic car model. SAE International Journal of Passenger Cars-Mechanical Systems, 7(2014-01-0607), 646-653, 2014.
18. Gritskevich, M. S., Garbaruk, A. V., Schtze, J., Menter, F. R.: Development of DDES and IDDES Formulations for the $k-\omega$ Shear Stress Transport Model. Flow, turbulence and combustion, 88(3), 431-449, 2012.
19. Heft, A., Indinger, T., & Adams, N., Investigation of unsteady flow structures in the wake of a realistic generic car model. In 29th AIAA Applied Aerodynamics Conference (p. 3669), 2011.
20. Heft, A. I., Indinger, T., & Adams, N. A. Introduction of a new realistic generic car model for aerodynamic investigations (No. 2012-01-0168). SAE Technical Paper, 2012.
21. Heft, A. I., Indinger, T., & Adams, N. A. (2012). Experimental and Numerical Investigation of the DrivAer Model, ASME 2012, July 8-12, 2012.
22. Hupertz, B., Chalupa, K., Lewington, N., Howard, K. et al., "On the Aerodynamics of the Notchback Open Cooling DrivAer: A Detailed Investigation of Wind Tunnel Data for Improved Correlation and Reference," SAE Technical Paper 2021 01 0958, 2021.
23. Jasak, H., Weller, H.G, and Gosman, A.D.: High resolution NVD differencing scheme for arbitrarily unstructured meshes, International Journal for Numerical Methods in Fluids, **31**, 431-449, 1999.
24. Kawai, S., Larsson, J. Wall-modeling in large eddy simulation: Length scales, grid resolution, and accuracy. Physics of Fluids, 24(1), 015105, 2012.
25. Launder, B. E. and Spalding, D. B., The Numerical Computation of Turbulent Flows, Computer Methods in Applied Mechanics and Engineering. 3. 269289, 1974.
26. Menter, F. R.: A new paradigm in Turbulence Modeling for Aerodynamic Simulations, ANSYS Webinar, 2016.
27. Menter, F. R.: Influence of freestream values on k-ω turbulence model predictions. AIAA J, 30(6), 1657-1659, 1992.
28. Menter, F. R.: Two-equation eddy-viscosity turbulence models for engineering applications. AIAA journal, **32(8)**, 1598-1605, 1994.
29. Menter, F. R., Kuntz, M.: Adaptation of eddy-viscosity turbulence models to unsteady separated flow behind vehicles. In The aerodynamics of heavy vehicles: trucks, buses, and trains. Springer Berlin Heidelberg, 339-352, 2004.
30. Menter, F. R., Egorov, Y.: The scale-adaptive simulation method for unsteady turbulent flow predictions. Part 1: theory and model
31. Menter, F. et al. Next generation Ansys GPU CFD solver technology for external aerodynamic applications, SIMVEC Congress, Baden-Baden, Germany, 2022.
32. Mirzaei, M., Krajnovic, S., Basara, B.: Partially-Averaged Navier–Stokes simulations of flows around two different Ahmed bodies, Computers & Fluids **117**, 273-286, 2015.
33. Mockett, C.: A Comprehensive Study of Detached-Eddy Simulation. Ph.D. thesis, TUB, 2009.
34. Peters, B. C., Uddin, M., Bain, J., Curley, A., & Henry, M, Simulating drivAer with structured finite difference overset grids (No. 2015-01-1536). SAE Technical Paper, 2015.
35. Piomelli, U., Balaras, E. Wall-layer models for large-eddy simulations. Annual review of fluid mechanics, 34(1), 349-374, 2002.
36. Poletto, R., et al. "Embedded DDES of 2D hump flow." Progress in Hybrid RANS-LES Modelling: Papers Contributed to the 4th Symposium on Hybrid RANS-LES Methods, Beijing, China, September 2011. Springer Berlin Heidelberg, 2012.
37. Rüttgers, M., Park, J., & You, D. Large-eddy simulation of turbulent flow over the DrivAer fastback vehicle model. Journal of Wind Engineering and Industrial Aerodynamics, 186, 123-138, 2019.
38. Shih, T. H., Liou, W. W., Shabbir, A., Yang, Z., & Zhu, J. A new k-epsilon eddy viscosity model for high reynolds number turbulent flows. Computers & Fluids, 24(3), 227-238, 1995.
39. Shinde, G., Joshi, A., & Nikam, K., Numerical investigations of the DrivAer car model using opensource CFD solver OpenFOAM. Tata Consultancy Services, Pune, India, 2013.
40. Shur, M. L., Spalart, P. R., Strelets, M. K., Travin, A. K. A hybrid RANS-LES approach with delayed-DES and wall-modelled LES capabilities. International journal of heat and fluid flow, 29(6), 1638-1649, 2008.
41. N. Simmonds, J. Pitman, P. Tsoutsanis, K. W. Jenkins, A. Gaylard & W. Jansen. Complete body aerodynamic study of three vehicles, SAE Technical Paper, ISSN 0148-7191, 2017.
42. Smagorinsky, J., General Circulation Experiments with the Primitive Equations. I. The basic Experiment, Monthly Weather Review **91**, 99-164, 1963.
43. Spalart, P. R., Jou, W. H., Strelets, M., Allmaras, S. R.: Comments on the feasibility of LES for wings, and on a hybrid RANS/LES approach. Advances in DNS/LES, **1**, 4-8, 1997.
44. Spalart, P.R., Strategies for turbulence modelling and simulations, International Journal of Heat and Fluid Flow 21, 252-263, 2000.

45. Spalart, Philippe R., and Craig Streett. Young-person's guide to detached-eddy simulation grids. No. NAS 1.26: 211032, 2001.
46. Spalart, P.R., Deck, S., Shur, M., Squires, K.D., Strelets, M., Travin, A.: A new version of detached-eddy simulation, resistant to ambiguous grid densities, Theor. Comput. Fluid Dyn. **20**, 181-195, 2006.
47. Sterken, L., Sebben, S., & Lofdahl, L.: Numerical Implementation of Detached-Eddy Simulation on a Passenger Vehicle and Some Experimental Correlation. Journal of Fluids Engineering, 138(9), 091105, 2016.
48. Strangfeld, C., Wieser, D., Schmidt, H. J., Woszidlo, R., Nayeri, C., & Paschereit, C. Experimental Study of Baseline Flow Characteristics for the Realistic Car Model DrivAer (No. 2013-01-1251). SAE Technical Paper, 2013.
49. S2A website: $https://www.soufflerie2a.com/moyens,soufflerie/soufflerie-echelle-11-561.html$.
50. Travin, A., Shur, M., Strelets, M., Spalart, P.R.: Physical and numericals upgrades in the Detached-Eddy Simulation of complex turbulent flows, Fluid Mechanics and its applications 65, 239-254, 2002.
51. Varney, M., "Base Drag Reduction for Squareback Road Vehicles," Loughborough University, 2019.
52. Varney, M., Passmore, M., Wittmeier, F., & Kuthada, T. Experimental Data for the Validation of Numerical Methods: DrivAer Model. Fluids, 5(4), 236, 2020.
53. Viher, J., Tibaut, P., Basara, B. and Krajnovic, S., Computational study of a car aerodynamics using the Partially-Averaged Navier-Stokes approach, In Aerovehicles 3, Milano, Italy, June 13-15, 2018.
54. Wang, S., Avadiar, T., Thompson, M. C., & Burton, D. Effect of moving ground on the aerodynamics of a generic automotive model: The DrivAer-Estate. Journal of Wind Engineering and Industrial Aerodynamics, 195, 104000, 2019.
55. Waudby-Smith, P., Bender, T., & Vigneron, R. The GIE S2A full-scale aero-acoustic wind tunnel (No. 2004-01-0808). SAE Technical Paper, 2004.
56. Wieser, D., Nayeri, C. N., & Paschereit, C. O. Wake structures and surface patterns of the drivaer notchback car model under side wind conditions. Energies, 13(2), 320, 2020.
57. Wolfshtein, M. The Velocity and Temperature Distribution of One-Dimensional Flow with Turbulence Augmentation and Pressure Gradient, Int. J. Heat Mass Transfer. 12. 301–318, 1969.